

Copyright © 1991, by the author(s).  
All rights reserved.

Permission to make digital or hard copies of all or part of this work for personal or classroom use is granted without fee provided that copies are not made or distributed for profit or commercial advantage and that copies bear this notice and the full citation on the first page. To copy otherwise, to republish, to post on servers or to redistribute to lists, requires prior specific permission.

**EFFECTS OF DC BIAS ON THE KINETICS  
AND ELECTRICAL PROPERTIES OF  
SILICON DIOXIDE GROWN IN AN ELECTRON  
CYCLOTRON RESONANCE PLASMA**

by

D.A. Carl, D.W. Hess, M.A. Lieberman, T.D. Nguyen,  
and R. Gronsby

Memorandum No. UCB/ERL M91/5

22 January 1991

**EFFECTS OF DC BIAS ON THE KINETICS  
AND ELECTRICAL PROPERTIES OF  
SILICON DIOXIDE GROWN IN AN ELECTRON  
CYCLOTRON RESONANCE PLASMA**

by

D.A. Carl, D.W. Hess, M.A. Lieberman, T.D. Nguyen  
and R. Gronsby

Memorandum No. UCB/ERL M91/5

22 January 1991

**ELECTRONICS RESEARCH LABORATORY**

College of Engineering  
University of California, Berkeley  
94720

TITLE PAGE

**EFFECTS OF DC BIAS ON THE KINETICS  
AND ELECTRICAL PROPERTIES OF  
SILICON DIOXIDE GROWN IN AN ELECTRON  
CYCLOTRON RESONANCE PLASMA**

by

D.A. Carl, D.W. Hess, M.A. Lieberman, T.D. Nguyen  
and R. Gronsky

Memorandum No. UCB/ERL M91/5

22 January 1991

**ELECTRONICS RESEARCH LABORATORY**

College of Engineering  
University of California, Berkeley  
94720

# Effects of dc bias on the kinetics and electrical properties of silicon dioxide grown in an electron cyclotron resonance plasma

D. A. Carl<sup>a</sup> and D. W. Hess, Department of Chemical Engineering

M. A. Lieberman, Department of Electrical Engineering and Computer Sciences

T. D. Nguyen<sup>1,2</sup> and R. Gronsky<sup>2</sup>

<sup>1</sup>Center for X-Ray Optics, Lawrence Berkeley Laboratory (LBL) and

<sup>2</sup>National Center for Electron Microscopy, LBL and  
Department of Materials Science and Mineral Engineering

University of California  
Berkeley, CA 94720

## Abstract

Thin (3-300 nm) oxides were grown on single crystal silicon substrates at temperatures from 523 K to 673 K in a low pressure electron cyclotron resonance oxygen plasma. Oxides were grown under floating, anodic or cathodic bias conditions, although only the oxides grown under floating or anodic bias conditions are acceptable for use as gate dielectrics in metal - oxide - semiconductor (MOS) technology. Oxide thickness uniformity as measured by ellipsometry decreased with increasing oxidation time for all bias conditions. Oxidation kinetics under anodic conditions can be explained by negatively charged atomic oxygen, O<sup>-</sup>, transport limited growth. Constant current anodizations yielded three regions of growth: 1) a concentration gradient dominated regime for oxides thinner than 10 nm; 2) a field dominated regime with ohmic charged oxidant transport for oxide thickness in the range of 10 nm to approximately 100 nm; and 3) a space-charge limited regime for films thicker than approximately 100 nm. The relationship between oxide thickness ( $x_{ox}$ ), overall potential drop ( $V_{ox}$ ) and ion current ( $j_i$ ) in the space-charge limited transport region was of the form:  $j_i \propto V_{ox}^2 / x_{ox}^3$ .

---

<sup>a</sup>Current Address: IBM General Technology Division, Dept. G 34, 1000 River Road, Essex Junction, VT 05452

Transmission electron microscopy analysis of 5 to 60 nm thick anodized films indicated that the silicon-silicon dioxide interface was indistinguishable from that of thermal oxides grown at 1123 K. High frequency capacitance - voltage (C-V) and ramped bias current - voltage (I-V) studies performed on 5.4 to 30 nm gate thickness capacitors indicated that the as-grown ECR films had high levels of fixed oxide charge ( $> 10^{11} \text{ cm}^{-2}$ ) and interface traps ( $> 10^{12} \text{ cm}^{-2} \text{ eV}^{-1}$ ). The fixed charge level could be reduced to  $\approx 4 \times 10^{10} \text{ cm}^{-2}$  by a 20 minute polysilicon gate activation anneal at 1123 K in nitrogen; the interface trap density at mid - bandgap decreased to  $\approx 1-2 \times 10^{11} \text{ cm}^{-2} \text{ eV}^{-1}$  after this process. The mean breakdown strength for anodic oxides grown under optimum conditions was  $10.87 \pm 0.83 \text{ MV cm}^{-1}$ . Electrical properties of the 5.4 to 8 nm gates compared well with thicker films and control dry thermal oxides of similar thicknesses.

## I. Introduction

Oxidation of silicon is a key process in metal-oxide-semiconductor (MOS) device fabrication. As the device gate area and gate thickness decrease and as processing moves from the traditional planar to the third dimension, formation of extremely thin gate dielectrics ( $< 10$  nm thick) with acceptable electrical properties becomes difficult with conventional thermal oxidation. Processing time-at-temperature (i.e., the thermal budget) is also an important consideration in current and future device fabrication due to the increased probability of silicon defect formation at elevated temperatures, as well as dopant redistribution or junction movement. Thus low temperature gate dielectric fabrication processes are needed. One approach to this problem has been the use of glow discharges to grow oxide on silicon.<sup>1-14</sup> (Reference 5 also addresses GaAs anodization at low temperatures, but the kinetics and transport processes are analogous to silicon plasma oxidation.) In the present study, oxygen or oxygen - containing electron cyclotron resonance (ECR) discharges were used to grow silicon dioxide from single crystal, p-type,  $\langle 100 \rangle$  oriented silicon wafers. An ECR discharge was used due to the higher ionization level (up to  $\approx 20\%$  in the source regions), complete power absorption at low (0.01 to 1 Pa) pressures and low (20-50 eV) ion bombardment energies. The kinetics of this growth process were analyzed via observation of the effects of discharge parameters and wafer bias upon the observed growth rates and film properties. Oxide films were subsequently analyzed chemically, physically and electrically to determine if they merit use as gate dielectrics in semiconductor devices. Results of these analyses indicate that negatively charged oxygen atoms formed at the plasma -  $\text{SiO}_2$  interface are the primary oxidant under anodic oxidation conditions. Transport relations for this ionic oxidant are developed from electric field measurements performed during the oxidation process.

## II. Experiment

The ECR system used in these experiments has been described previously.<sup>14,15</sup> A 2.45 GHz, 800 W CW microwave power supply/matching network was connected by a WR284 rectangular

waveguide through a quartz window to the 7.8 cm diameter by 22 cm long stainless steel cylindrical vacuum chamber. No special microwave mode conversion was used. Two electromagnets driven in a mirror configuration established the axial B field required for cyclotron resonance. Single crystal (p-type, 10-15  $\Omega$  cm, <100> orientation) silicon wafers 75 mm in diameter were clamped onto an aluminum holder via a retention ring. The aluminum holder was located 14 cm from the source chamber and contained resistive heating elements and a thermocouple for substrate temperature measurement and control. The substrate holder was designed for floating or dc bias operation. As shown in Fig. 1, a 3.2 mm thick quartz plate covered the metal portions of the sample holder assembly and had a 50 mm diameter opening to the discharge centered 7 mm above the wafers. Thus all net dc current flowing in the system was forced to flow through the center 50 mm of the 75 mm wafers. Optical emission spectroscopy (OES) was used to monitor plasma emission and to aid in power tuning optimization. This system was also used to perform actinometry on the relative gas phase atomic oxygen concentration,  $[O]/[O_{ref}]$ , as a function of various plasma parameters using the 750.4 nm  $Ar^+$  emission line as a reference.<sup>15,16</sup> The standard  $[O_{ref}]$  used in these studies was the concentration of atomic oxygen in our system in a pure oxygen discharge at 0.13 Pa and 500 W forward power. A 0.076 mm diameter Langmuir probe was used to determine plasma densities ( $n_i$ ) and electron temperatures ( $T_e$ ) as functions of radial and axial position, pressure, power and plasma composition, as described in detail in ref. 17.

Prior to oxidation, wafers were cleaned in a boiling sulfuric acid and hydrogen peroxide solution for ten minutes, rinsed, immersed in 10:1 buffered oxide etchant (BOE) until hydrophobic, then rinsed to 16 M $\Omega$ -cm in DI water. The procedure for film growth was identical to ref. 14, except that bias was applied to the substrate prior to plasma ignition. Care was taken to ensure each wafer was aligned with the primary flat located at a fixed position in the sample holder, to allow for run - to - run thickness uniformity comparisons. The net film thickness for a given time under the same plasma conditions was not affected by repeatedly stopping the oxidation, removing the film and measuring the physical properties. This was determined by oxidizing 3 to 5 wafers at different times

and then comparing the growth rates with a single wafer oxidation, stopping at each of these times. Each data set contains oxidation information from at least three wafers. Fourier transform infrared spectroscopy (FTIR), x-ray photoelectron spectroscopy (XPS), Auger electron spectroscopy (AES), transmission electron microscopy (TEM), ellipsometry (Gaertner model L116A, HeNe laser, single wavelength system) and oxide etch rates in 5:1 buffered oxide etchant (BOE) were used to characterize the physical and chemical properties of the oxides. The ellipsometric measurements were performed on an 18 point fixed grid inside of the 50 mm oxidation area, in a manner similar to ref. 8, at both fixed (film thicknesses < 15 nm) and variable (i.e. the ellipsometric solution for simultaneous solution of thickness and refractive index) indices of refraction.

Cross - sectional TEM samples were prepared by mechanical thinning to approximately 30  $\mu\text{m}$ , followed by ion beam milling on a cold stage at 5 kV. The samples were studied in a JEOL - JEM 200CX electron microscope with a high resolution goniometer operating at 200 kV. The electron beam was parallel to the <100> crystal plane of the silicon surface.

Metal - oxide - semiconductor (MOS) capacitor structures (100 x 100  $\mu\text{m}$  squares) were fabricated lithographically from evaporated aluminum (400 nm thick) or deposited  $\text{n}^+$  polysilicon on top of the oxides. The polysilicon was deposited at 50 Pa and 923 K for 1.5 hours and activated at 1123 K for 20 minutes in dry atmospheric pressure  $\text{N}_2$ . Polysilicon film thickness was 500 nm. Capacitance - voltage (C-V) data were obtained using an HP 4280A 1 MHz Capacitance Meter/C-V Plotter connected to an HP 9836U computer prior to and after a 673 K, 30 minute sinter in an  $\text{N}_2/\text{H}_2$  atmosphere gas. Bias temperature stress was performed at fields of  $\pm 2 \text{ MV cm}^{-1}$  at 573 K for 4 minutes. Interface trap densities,  $D_{it}$  ( $\text{cm}^{-2} \text{ eV}^{-1}$ ) were evaluated at mid bandgap. The current - voltage (I-V) testing was performed with dc ramped voltage sweeps from an HP 4145B Semiconductor Parameter Analyzer. Cumulative breakdown vs. applied field curves were constructed from I-V tests of at least 25 capacitors located at random wafer locations. Breakdown field was defined as the field required to pass 1  $\mu\text{A}$  through the defined gate.

### III. Discharge Characteristics

In any kinetic study, it is critical to measure or estimate the fluxes of reacting species to the substrate prior to establishing the validity of postulated rate expressions. In plasma processing, many reactions are initiated or catalyzed by electron or ion bombardment. Therefore, a measurement of electron and ion fluxes to the surface under the various processing conditions is required along with measurements/estimates of the gas phase reactant composition. Previous Langmuir probe studies in this system<sup>14,15,17</sup> yielded the following results: 1) Ion density, ( $n_i$ ), measured at the wafer position was linear with input power from  $P_{\text{forward}}$  of 150 W to 750 W. 2) Maximum oxygen ion flux ( $\text{O}_2^+$  and  $\text{O}^+$ ) was observed with a magnet coil current of 150 A, which corresponded to the largest volume resonance zone located in the magnetic mirror midplane in the source chamber.<sup>14,17</sup> 3) To a first approximation,  $n_i$ , electron temperature, ( $T_e$ ), and floating potential ( $V_f$ ) were roughly constant for mixtures of  $\text{O}_2$ , Ar,  $\text{N}_2$  and  $\text{H}_2$  at pressures near 0.013 Pa.<sup>15</sup> From these data, the fluxes of positive ions and electrons to the wafer at any operating condition can be estimated.

Ion and electron fluxes are only part of the picture, however. The gas phase neutral reactant flux is also important. As we did not have a direct means of quantitatively measuring gas phase composition during oxidation, OES was used to identify emitting species in the discharge and actinometry was used to obtain a relative value of atomic oxygen concentration as a function of operating conditions. Results of the actinometry studies can be summarized as follows:<sup>15</sup> 1) for pure oxygen discharges in the 0.013 Pa to 1 Pa range, the concentration of atomic oxygen increases linearly with increasing pressure, holding all other input parameters constant; and 2) for all gas mixtures tested in the 0.07 to 0.26 Pa pressure range, the concentration of atomic oxygen, [O], is approximately proportional to the partial pressure of  $\text{O}_2$  in the feed stream. This information, combined with the Langmuir probe data, sets the flux of reacting species (atomic and molecular ions, atomic oxygen, and electrons) to the substrate during the oxidation process.

When the wafer is floating in the discharge, no net current is flowing, i.e., ion and electron fluxes to the wafer surface are equal. When a dc bias is applied to the wafer holder, the surface

exposed to the discharge acts as a large planar Langmuir probe<sup>18,19</sup> and current is drawn through the wafer and the growing oxide film. A typical wafer holder dc I-V curve is shown in Fig. 2. This characteristic is sensitive to plasma conditions through  $n_i$  and  $T_e$ .<sup>18,19</sup> Figure 2 also shows that the measured ion density 1 cm from the wafer holder is not affected by the wafer dc bias. Furthermore, the ion density in the source region is also unperturbed by the wafer bias (as determined by the 525 nm  $O_2^+$  OES signal, which has been shown to be linearly proportional to  $n_i$  in our system<sup>14</sup>); thus we assume that the wafer holder can be independently biased over this potential range with no resulting change in  $n_i$ ,  $T_e$ , or ion energy in the ECR plasma.

#### IV. Bias Application and Measurement of Electric Field in the Oxide

Figure 1 shows a schematic of the dc bias system and Fig. 3 illustrates the potential profiles in the growing oxide as a function of the applied bias. As mentioned previously, the wafer surface can be thought of as a large, planar Langmuir probe. Therefore, for a given initial current and set of system conditions there will be a corresponding substrate surface potential,  $V_s$ , as shown in Fig. 3.  $V_s$  will be equal to the applied voltage,  $V_{app}$ , only at this initial condition, i.e., for bare silicon or for oxides that are too thin to prevent surface charging. (For the temperatures of oxidations performed in this study, it has been assumed that the conductivity of silicon is significantly higher than that of the growing oxide film; thus, the entire potential drop will be across the growing film and the plasma sheath.) For the constant current case (positive or negative current),  $V_s$  is fixed and  $V_{app}$  must be changed with increasing oxide thickness in order to maintain the anodization current,  $j$ , at the initial value. The rate of change of  $V_{app}$  with the oxide thickness will depend upon the oxide properties. For the most simple case (ohmic behavior), the overall field in the oxide at a particular oxide thickness will be:

$$E_{ox} = \frac{V_{app} - V_s}{x_{ox}} = \frac{j}{\sigma} \quad (1)$$

where  $E_{ox}$  is the oxide field,  $x_{ox}$  is the oxide thickness,  $j$  is the anodization current density ( $j=r$ ) and  $\sigma$  is the overall conductivity of the current carriers in the oxide. Electrons are by far the majority charge carriers during anodization (as will be shown in Section V), thus  $\sigma$  is essentially the electron conductivity in the oxide.

For constant applied voltage, the field in the oxide cannot be determined directly. Initially,  $V_s = V_{app}$ , as was the case with constant current operation. After the oxide has reached a thickness that is large enough to sustain a field,  $V_s$  will begin to move towards the floating potential value of the surface at large oxide thickness,  $V_f$ .  $V_s$  will therefore change with time as a function of oxide thickness and oxide properties. If the oxide grown under this bias condition is physically, chemically and electrically similar to the oxide grown under constant current conditions, then  $V_s$  can be estimated from Eq. (1) using a conductivity obtained during constant current anodizations. If the transport is not ohmic, then the sample holder IV curve can be used to estimate  $V_s$  from the measured current drawn at any time and oxide thickness. This calculation is based upon the assumption that the work function difference between the oxide surface and the holder surface is small and can be neglected.

The field in the film during floating operation is much more difficult to estimate. Even though the net current is zero, there is a substantial flux ( $\approx 10\text{-}20 \text{ mA cm}^{-2}$ ) of ions and electrons to the surface of the growing film.<sup>15</sup> It is well known that uv photons effectively create positive charge in an oxide exposed to the plasma. Such charge in the film can establish internal fields that attract negative surface charge and help drive the diffusion process. This general idea has been used in the formulation of several models of charged oxidant transport<sup>20,21</sup> and could explain why oxidation rates under floating conditions in ECR systems are at least an order of magnitude greater than what has been measured for uncharged atomic oxygen oxidation<sup>8</sup> or the rate measured on portions of the wafer outside of the plasma flux (i.e., blocked by the quartz shield) in ECR systems<sup>12,14</sup>. Unfortunately, this internal field can only be postulated; it could not be measured in our system.

## V. Oxidation Results

### A. Negative Bias Case

As is the case for aluminum<sup>18</sup>, Nb, or Pb<sup>10</sup>, silicon can be oxidized under bias conditions that attract positive ions, i.e. under cathodic conditions.<sup>4</sup> This bias condition also permits injection of electrons from the silicon substrate through the growing oxide to the plasma. FTIR analysis confirmed that SiO<sub>2</sub> could grow in our system for dc applied biases that were more negative than  $V_f$ , (e.g.  $V_{app} < -15$  V at 0.13 Pa) but the quality of the oxides as determined by BOE etch rates (1.5 to 3 times faster than thermal oxide etch rate), ellipsometry (refractive indices of 1.43 or below, uniformity  $\pm 30$  % or more, one standard deviation) and electrical measurements (breakdown fields of  $1-7$  MV cm<sup>-1</sup>  $\pm 3$  MV cm<sup>-1</sup>), was poor and not reproducible. These observations are similar to the results of near floating potential (i.e., low anodization current) operation in ref. 3. Consequently, any detailed kinetics analysis would be questionable. Qualitatively, the following trends were observed:

- 1) For  $(V_f - 15 \text{ V}) < V_{app} < V_f$ , oxides grew at rates similar to the floating potential rate, but stopped at some thickness, similar to the thermal oxidation bias experiments of Jorgensen.<sup>22</sup> The termination thickness was only reproducible for small values of  $|V_{app}| - |V_f|$ . For example, at 0.13 Pa, 500 W  $P_{forward}$  and  $V_{app} = -20$  V ( $|V_{app}| - |V_f| = 5$  V), the oxide grew to approximately 40 nm in 120 minutes, after which the rate effectively decreased to near zero.
- 2) For  $V_{app} \ll V_f$  ( $\approx 35$  V or more negative), a 5 nm oxide formed in 1-2 minutes, but did not increase in thickness with oxidation times to 120 minutes. These observations suggest that positively charged oxygen ions cannot account for the silicon oxidation observed. If positive ions alone were responsible for the oxidation process, one would expect an oxidation rate that is proportional to the positive current drawn, i.e., proportional to the flux of reactant. Instead, oxide grows for only a limited range of negative bias. This result might be explained by recently proposed models of electron-active oxidation.<sup>23,24</sup> In these models, electrons are assumed to be injected from the silicon into the near-silicon oxide, where they can attach (possibly dissociatively) to interstitial oxygen to form O<sup>-</sup>. The negatively charged oxygen which is assumed to be smaller than molecular oxygen and is apparently much more reactive, can then

diffuse towards the interface and react with the bulk silicon, as long as the fields in this region are not strong enough to overcome the concentration gradient driving force. When the negative field becomes too high, this process stops. Although such a model can explain these observations, the non-reproducibility of the results and the poor quality of the oxides grown indicate that this bias regime should not be used in a gate dielectric oxidation process.

## B. Floating Case

As shown previously,<sup>7</sup> silicon oxides with reasonable physicochemical properties can be grown under floating conditions in ECR discharges. Fig. 4 shows oxide thickness vs. oxidation time data at four temperatures for a  $P_{\text{forward}} = 500$  W, 0.13 Pa pure oxygen discharge. In the initial oxidation regime, no measurable difference in growth rate was observed for changing substrate temperatures. For oxides under 30 nm thickness, a simple power law model fit the data most accurately. Indeed, if one assumes that the initial film growth is purely diffusion limited, then the initial rate can be expressed as:

$$\text{Rate} = \frac{dx_{\text{ox}}}{dt} = k_1 r_{i^-} - k_2 D_{i^-} \frac{dn_{i^-}}{dx_{\text{ox}}} \quad (2)$$

where  $r_{i^-}$  is the flux of  $O^-$  ions through the oxide,  $(dn_{i^-} / dx_{\text{ox}})$  is the concentration gradient of the reactant in the film,  $D_{i^-}$  is the solid state diffusivity of the ion, and  $k_1$  and  $k_2$  are physical constants that correct for stoichiometry and oxide density. For  $\text{SiO}_2$ ,  $k_1 = 83 \text{ nm cm}^2 \text{ mA}^{-1} \text{ min}^{-1}$ . If we assume that the near-surface concentration of reactant remains constant (i.e. it is in equilibrium with the plasma phase) over the oxidation, that all  $O^-$  transported across the oxide instantaneously reacts, and that the concentration gradient is linear, Eq. (2) can be simplified to:

$$\frac{dx_{\text{ox}}}{dt} = \frac{k_3 D_{i^-} n_{i^-, \text{sur}}}{x_{\text{ox}}} = \frac{k_4}{x_{\text{ox}}} \quad (3)$$

where  $n_{i, \text{sur}}$  is the concentration of  $O^-$  near the oxide surface. Eq. (3) is the classical parabolic rate equation with solution:

$$x_{\text{ox}}(t) = \left( k_5 t + x_{\text{ox}}^2(t=0) \right)^{\frac{1}{2}} \quad (4)$$

Applying Eq. (4) to the oxide thickness below 30 nm, we obtain a value of  $6.14 \text{ nm}^2 \text{ min}^{-1}$  for the constant  $k_5$ . This fit is also shown in Fig. 4. The intercept for this regression ( $r^2 = 0.997$ ) was 6.2 nm, significantly higher than the native oxide thickness of 1.4 nm. It will be shown below that this intercept is similar to that obtained from a regression analysis of constant current oxidation data. Therefore, it appears that this oxide thickness grows almost instantaneously (i.e.,  $t < 0.33 \text{ min}$ ) in our system, regardless of the wafer bias at pressures below 1.3 Pa.

Unlike the results of Kimura and co-workers<sup>7</sup>, we observe that the oxide displays a marked change in growth rate after the film reaches approximately 30 nm in thickness. This may be due to several factors. First, the film becomes much less uniform as the floating case oxidation proceeds, as shown in Fig. 4. Also, the etch rate of the film in BOE solutions increases from 1.5 times the thermal oxide rate to over 2 times the rate in this thickness region. It is therefore believed that the apparent jump in oxidation rate is an artifact of the film properties.

The apparent activation energy for oxidation under floating bias conditions is below the resolution of our measurements and therefore is effectively zero. This was observed in our previous study for similar oxidation conditions<sup>14</sup>. This may be due to the low activation energy of ion diffusion combined with surface heating from the discharge. It may also be due to the adsorption/desorption equilibrium energetics, which can substantially decrease an apparent activation energy. It should be noted that the excellent fit to a strictly concentration gradient driven solution does not rule out the possibility of field enhanced transport. If a large amount of fixed positive charge is generated in the film during the growth cycle, the subsequent field enhancement could mask any temperature dependence of oxidant transport. This build-up of positive charge in the oxide may also explain the apparent increase in oxidation rate for films thicker than 30 nm, i.e., the field enhancement may

become much more important than the concentration gradient when large amounts of positive charge have built up in the oxide.

### C. Positive Bias Case

The oxides with the best thickness uniformity, physical and electrical characteristics were grown under anodic conditions. Two types of anodizations were performed in this study: constant current and constant applied voltage. As explained in Section IV, constant current oxidation can yield a direct measurement of the field in the oxide and thus allow determination of the conductivity in Eq. (1). For pressures ranging from 0.13 to 1.3 Pa, the film thickness uniformity varied from 2-5% (one standard deviation) over the 18 point grid for films less than 100 nm, gradually increasing to 5-10% for thicker oxides. The thickness uniformity was slightly worse for the 0.033 Pa case, ranging from 5-10% for films less than 100 nm in thickness, increasing to  $\approx 15\%$  above this thickness.

#### 1. Constant Current Anodization

For constant current anodization, a positive bias with respect to the floating potential is applied to the backside of the wafer, and voltage is allowed to vary with time to maintain a given negative current. Fig. 5 shows a log-log plot of oxide thickness vs. time for constant anodization current of  $-20 \text{ mA cm}^{-2}$  at 623 K,  $P_{\text{forward}} = 500 \text{ W}$ , and four different pressures. Temperatures were varied from 523 K to 673 K with no change in growth rate, but with slightly different  $V_{\text{app}}(t)$ . It was assumed that these minor differences were due to the change in conductivity with temperature.<sup>25</sup> Three regions are clearly visible for all data shown in Fig. 5: 1) the initial oxidation regime ( $x_{\text{ox}} < 10 \text{ nm}$ ) that appears to follow the kinetics predicted by Eq. (4); 2) a linear growth rate region from  $10 \text{ nm} < x_{\text{ox}} < 100 \text{ nm}$  where the oxide appears ohmic; and 3) a decrease in oxidation rate past  $x_{\text{ox}} > 100 \text{ nm}$ , possibly due to space-charge limitations<sup>5,10,11,18,19</sup>.

Eq. (4) was used to analyze the initial oxidation regime. In this regime, the film thickness is too small to support a large potential drop, as seen in the  $(V_{\text{app}} - V_s)$  vs. time profiles in Fig 6. Figure 6 shows that there is an induction period at the start of the anodization where  $(V_{\text{app}} - V_s)$  does not change with changing film thickness. This behavior has been observed in other systems.<sup>10,11</sup> Data

analyses via least squares regression are shown as solid lines in Fig. 5. All regression  $r^2$  values were  $\geq 0.99$ . The values for  $k_5$  and  $x_{\text{ox}}(t=0)$  are listed in Table I. As observed under floating potential operation,  $x_{\text{ox}}(t=0)$  is on the order of 4 nm for the 0.033 Pa, 0.13 Pa, and 0.23 Pa cases. The  $x_{\text{ox}}(t=0)$  value for the 1.3 Pa anodization was closer to the native oxide thickness. This is indicative of a very rapid (i.e.,  $< 0.33$  min) oxidation process for thin ( $< 4$  nm) films that is not yet understood. The parabolic rate constant,  $k_5$ , varied from  $29.38 \text{ nm}^2 \text{ min}^{-1}$  at 0.033 Pa to  $13.82 \text{ nm}^2 \text{ min}^{-1}$  at 0.260 Pa. These values are close to the parabolic rate constant observed for the 0.13 Pa floating potential case, but consistently higher. This may be due to a higher near-surface concentration of negatively charged atomic oxygen under positive bias conditions, i.e., the near-surface concentration may scale with the electron flux from the plasma. The variations of  $k_5$  and  $x_{\text{ox}}(t=0)$  with pressure roughly track the electron temperature<sup>15</sup>, indicating the electron energy may be important in the formation of the oxidant. The type of electron temperature dependence has been observed in other plasma oxidation systems.<sup>5</sup>

Once the film has reached approximately 10 nm in thickness,  $(V_{\text{app}} - V_s)$  had to be increased with time to maintain the constant anodization current. During the period from  $x_{\text{ox}} = 10$  nm to  $x_{\text{ox}} \approx 100$  nm, the film grows with a constant rate, and  $(V_{\text{app}} - V_s)$  rises linearly with time. Thus, from Eq. (1) the film is ohmic in this region. Eq. (2) can be amended to include field-induced ionic transport by adding the ohmic transport term  $\eta \sigma E_{\text{ox}}$ :

$$\frac{dx_{\text{ox}}}{dt} = k_1 \Gamma_{i-} - \frac{k_4}{x_{\text{ox}}} + k_1 \eta \sigma E_{\text{ox}} \approx k_6, \text{ constant current, ohmic region} \quad (5)$$

where  $k_6$  is the linear rate coefficient for constant current oxidation in the ohmic region and  $\eta$  is the current efficiency, defined as:

$$\eta = \frac{\Gamma_{i-}}{\Gamma_{i-} + \Gamma_e} \approx \frac{\Gamma_{i-}}{\Gamma_e} \quad \text{for } \Gamma_{i-} \ll \Gamma_e \quad (6)$$

where  $r_e$  is the electron current in the film. It is assumed that the diffusion term,  $k_d/x_{ox}$  is negligible for  $x_{ox}$  above 10 nm. Table I lists the linear rate coefficients and the current efficiencies obtained from a linear regression analysis of the data in Figs. 5 and 6. Our linear rate coefficient values are similar to those observed by Pulfrey and Riche<sup>3</sup> in an inductively coupled rf plasma oxidation system for similar current densities. Current efficiencies were on the order of  $1 \times 10^{-3}$  for all cases;  $\eta$  is typically much less than 1% in silicon or gallium arsenide anodization.<sup>2,3,5,10,11,19</sup> It should also be noted that the overall conductivity calculated from Eq. (1) and the constant current anodization data was  $\approx 4 \times 10^{-9} \Omega^{-1} \text{ cm}^{-1}$ . This value is equal to that measured in thermal oxide conductivity experiments.<sup>25</sup> The linear rate coefficient,  $k_g$  had values ranging from 1.74 to 2.45 nm min<sup>-1</sup>, with the maximum value occurring at 0.13 Pa - the same pressure that plasma ion (and electron) density is maximum.

For film thicknesses greater than approximately 100 nm, the growth rate of the film is no longer constant in time. It has been shown that space-charge in a growing oxide can be responsible for non-linear growth kinetics of thick oxide films during constant current anodization.<sup>5,10,11,19,20</sup> Since the current is held constant during the entire oxidation process, the current efficiency from Eq. (5) must decrease in this regime.<sup>5,10,11</sup> Wolters and Zegers-van-Duynhoven (WZ)<sup>21</sup> showed that a power law relationship is one way of correlating ion hopping conduction coupled with space-charge limited transport growth data. Thus, oxide thickness in the space-charge region was fit to the following relation:

$$x_{ox} = C^* t^\alpha \quad (7)$$

where  $C^*$  is an effective rate coefficient and  $\alpha$  is a measure of the barrier height induced by the space-charge on the ion flux. Table I lists the constants obtained from linear regression of the data in Fig. 5. It is difficult to compare these values to thermal oxidation values or to the values obtained in our previous study<sup>14</sup> due to the substantial hopping conduction barrier height reduction in a large electric field. This information combined with the  $(V_{app} - V_s)$  vs. time data can then be used to calculate the

current efficiency as a function of time for a given anodization condition and therefore as a function of oxide field and thickness.

Space-charge effects are manifested under constant current conditions by non-linear increases in applied potential as film thickness increases.<sup>26,27,28</sup> The scaling of applied voltage with oxide thickness in the space-charge region for our constant current anodizations was:  $(V_{app}-V_s) \propto x_{ox}^{1.3}$ . Some previous studies indicated that this scaling was linear, although space-charge limited transport was invoked to explain the growth kinetics.<sup>10,11,19</sup> Another study showed non-linear oxide potential drops as functions of oxide thickness<sup>2</sup> but linear growth kinetics for constant current operation.<sup>3</sup> Our oxide voltage vs. oxide thickness to the 1.3 power scaling result is close to the theoretical value of space-charge limited ion transport for a constant ion mobility, i.e., Cobine's Law<sup>27</sup>, for which  $(V_{app}-V_s) \propto x_{ox}^{1.5}$ . The regression analysis of the data leading to the exponent of 1.3 includes points that are not in the fully developed space-charge limited growth regime, and thus underestimates the actual exponent. (This was not the case for constant applied bias anodizations, as will be shown in subsection C, where the exponent of 1.5 well fits the estimated  $(V_{app}-V_s)$  vs.  $x_{ox}$  data for films thicker than  $\approx 30$  nm.) Thus, the kinetics and the applied voltage vs. time data are consistent with space-charge limited growth in this regime.

## 2. Admixtures with Ar, H<sub>2</sub>, N<sub>2</sub> and N<sub>2</sub>O: Source of O<sup>-</sup>

Under low pressure conditions with modest sheath potentials (10-30 V), it is unlikely that O<sup>-</sup> from the plasma phase has sufficient energy to surmount the plasma sheath potential barrier and reach the substrate. It is most probable that the oxidant O<sup>-</sup> is formed on the surface of the growing film.<sup>5,18,29</sup> A simple surface reaction model can be proposed to estimate the surface concentration of O<sup>-</sup>. This model assumes that: 1) There is an equilibrium between the plasma phase and the substrate surface with respect to atomic oxygen, thus the surface concentration of adsorbed atomic oxygen is proportional to the plasma phase atomic oxygen partial pressure. 2) O<sup>-</sup> is formed when an adsorbed oxygen atom attaches an electron from the incoming flux of plasma electrons via the reaction:<sup>29</sup>



where  $O_{ad}$  is the adsorbed atomic oxygen and  $O_{ad}^-$  is the adsorbed  $O^-$ . 3)  $O_{ad}$  can also be consumed by the surface recombination reaction:



4) Under pseudo-steady state operation, the rate of generation of  $O^-$  via Eq. (8) is equal to the rate of  $O^-$  consumed in the oxidation reaction. To estimate the rate of  $O^-$  formation, the surface concentration of  $O_{ad}$  must first be calculated. The surface concentration of  $O_{ad}$ ,  $n'_{O}$ , can be found by application of the pseudo steady state assumption:

$$\frac{dn'_{O}}{dt} = r_{O^-} - Kn'_{O}{}^2 = 0; n'_{O} = \left( \frac{r_{O^-}}{K} \right)^{\frac{1}{2}} = K'[O]^{\frac{1}{2}} \quad (10)$$

where  $K$  is the recombination reaction rate coefficient in Eq. 9. Using Eq. (10) and Eq. (8), the rate of formation of  $O^-$  on the surface is:

$$\frac{dn'_{O^-}}{dt} = K'' r_e n'_{O^-} - K''' r_e [O]^{\frac{1}{2}} \quad (11)$$

where  $K''$  is the reaction rate constant for  $O^-$  formation and  $r_i$  can be directly related to the oxidation rate via Eq. (2). Thus, holding all surface conditions constant, the reaction rate should be proportional to the square root of the atomic oxygen concentration in the gas phase.

To test this hypothesis, constant current anodizations ( $-20 \text{ mA cm}^{-2}$ ) were performed at 0.13 Pa and  $P_{\text{forward}}=500 \text{ W}$  with admixtures of an inert gas (argon) and oxygen. The subsequent linear rate coefficient in the ohmic region of growth vs. actinometrically measured relative atomic oxygen concentration is shown in Fig. 7. Data from pure oxygen runs at different powers (and thus different atomic oxygen concentrations due to different electron densities) are also shown in Fig. 6. The same data plotted against the square root of the relative atomic oxygen concentration exhibit excellent agreement with Eq. (11).

While this model accounts for the linear oxidation rate for admixtures of argon at 0.13 Pa, it does not accurately predict the linear rate coefficients for other surface conditions. This can be seen by examining the linear rate coefficients listed in Table I. If Eq. (11) were valid at different total pressures, then the linear rate at 1.3 Pa should be 2.65 times greater than the 0.13 Pa rate for the same electron current (assuming that  $\eta$  is essentially constant) based upon a roughly sevenfold greater atomic oxygen concentration, as measured by actinometry. Clearly, this is not the case. Indeed, the two rates vary by a factor of only 1.5. Eq. (11) and the assumptions leading to it do not consider alternate mechanisms for adsorbed oxygen losses, adsorbed ion recombination, or the dependence of the rate constants on electron temperature. As electron temperatures increase considerably with decreasing pressure in our system<sup>15</sup>, this cross-sectional dependence could be of major importance.

Admixtures with H<sub>2</sub>, N<sub>2</sub> and N<sub>2</sub>O were also performed in this study. A high pressure (> 13 Pa) anodization study indicated that additions of small amounts ( $\approx$  1 %) of H<sub>2</sub> to the plasma during anodization decreased the anodization rate more than what would be expected by dilution.<sup>11</sup> It was assumed that H<sub>2</sub> can react with gas phase O<sup>-</sup> to form water and an electron, thus decreasing the gas phase O<sup>-</sup> concentration and therefore decreasing the rate.<sup>11</sup> This, of course, assumes that the flux of O<sup>-</sup> from the gas phase controls the oxidation rate. The addition of 1% of H<sub>2</sub> did not measurably affect our anodization rate. Higher concentrations (> 10%) of H<sub>2</sub> did measurably change the anodization rate in our system. The admixture rate was slightly lower than that predicted using Eqs. (8) - (11) most probably due to the reactive nature of the hydrogen atom. Hydrogen atoms not only take up surface adsorption sites, but also react with adsorbed atomic oxygen to form OH and water, thus reducing the supply of O<sub>ad</sub> and decreasing the rate predicted from Eq. (11).

Small additions of N<sub>2</sub>O have been shown previously to decrease the anodization rate at higher pressures.<sup>11</sup> In this case, it was assumed that N<sub>2</sub>O reacts with O<sup>-</sup> in the gas phase, yielding O<sub>2</sub><sup>-</sup> and NO in a two step process. The observed rates for additions of small ( $\approx$  10%) amounts of N<sub>2</sub>O did not measurably affect the anodization rate more than what would be expected from dilution. Indeed, oxides could be grown in pure N<sub>2</sub>O, indicating that gas phase gettering of O<sup>-</sup> had little effect at low

pressures.

Results from higher pressure (130 Pa) downstream oxidation of silicon indicate that addition of small amounts of  $N_2$  to the plasma can increase the oxidation rate by increasing atomic oxygen production.<sup>30</sup> Mixtures with  $N_2$  in our system yielded results similar to those seen in the addition of Ar,  $H_2$  and  $N_2O$ . Furthermore, as discussed in Section III,  $[O]$  was essentially linear with  $O_2$  admixture concentration as measured by actinometry at this pressure. Thus, the enhancement of atomic oxygen formation observed in higher pressure systems does not occur at low pressures in our system, where gas phase collisions are substantially reduced. It is interesting to note that the films grown in the  $H_2$  and Ar admixtures exhibited physical and chemical properties close to the pure  $O_2$  ECR oxides, while the  $N_2$  and  $N_2O$  admixture films had much higher etch rates (1.5 to 4 times the thermal oxide and pure  $O_2$  ECR oxide rates) in BOE and lower refractive indices ( $< 1.45$ ). FTIR analysis indicated that all films grown in the various admixtures were silicon dioxide, i.e., the  $N_2$  and  $N_2O$  admixture films did not exhibit any detectable oxynitride bonding and Si-H bonding was not detectable in the  $H_2$  admixture films.

### 3. Constant Applied Voltage

The results of two constant applied voltage anodizations are shown in Fig. 8. Oxide thickness vs. time could not be accurately modelled by a single rate expression; a piece-wise numerical fit was used to construct the solid lines in Fig. 8. As this anodization scheme does not allow for accurate measurement of the field in the oxide, the only available raw data for analysis is the oxide thickness vs. time data and the total negative current drawn vs. time data. From Eqs. (5) and (6), we have established that the oxidation rate is a linear function of the total negative current if the current efficiency,  $\eta$ , is constant. If this is true, a plot of the oxidation rate vs. negative current drawn should yield a straight line of slope  $k_1\eta$ . Fig. 8 shows this plot for the two constant voltage cases examined. For total currents less than  $8 \text{ mA cm}^{-2}$ , this relation yields a straight line, with a current efficiency of  $1.6 \times 10^{-3}$  for the grounded case and  $1.3 \times 10^{-4}$  for the +5 V case; these values are very close to the constant current efficiencies in the linear growth regions. The slope of the rate vs. electron current

plot decreases for currents larger than  $8 \text{ mA cm}^{-2}$ , indicating a slightly lower efficiency ( $\approx 0.78 \times 10^{-3}$ ). This difference is minor and may be an artifact of the numerical means of calculating the oxidation rate for small oxide thickness, when the current is highest.

Although the oxide field could not be directly measured in this anodization mode, an estimate of the field can be made through application of the following assumption: The total current drawn at any given oxide thickness can be related to the surface potential  $V_s$  via the holder IV characteristic for the plasma conditions used during the anodization. This again assumes that the holder-silicon-oxide system is acting as a large area Langmuir probe, and that the current drawn from the plasma is purely a function of the  $V_s$  of the probe. Therefore, the overall field in the oxide for any given  $x_{\text{ox}}$  and  $j$  was calculated from the first portion of Eq. (1),  $E_{\text{ox}} = (V_{\text{app}} - V_s) / x_{\text{ox}}$  (The potential profile as a function of position in the film was still unknown and we had no means of measuring the profile with our apparatus.)

If the charged particle transport is ohmic, then a plot of the product of total current and oxide thickness ( $j_{\text{T}}(t) x_{\text{ox}}(t)$ ) vs. the estimated oxide field ( $E_{\text{ox}}(t)$ ) should yield a straight line with a positive slope related to  $\eta$  and  $\sigma$ . The top portion of Fig. 9 shows this relation and has several interesting features. The initial retrograde ( $j_{\text{T}}(t) x_{\text{ox}}(t)$ ) vs.  $E_{\text{ox}}$  behavior is due to an observed (and not yet understood) slight initial increase in current density with increasing film thickness and has been observed elsewhere.<sup>10,11</sup> Past this initial region, the slope levels off to a near-zero value, and becomes negative at longer times. Clearly, this is not indicative of ohmic transport.

Previous workers have modified the solid-state hopping conduction model of Verwey<sup>31</sup> to include the effects of space-charge.<sup>19,21,26</sup> This modification includes a term accounting for local increases (and subsequent decreases in the opposite direction) in the barrier height for hopping conduction.<sup>21,26</sup> This model leads to an expression for the local flux of the ions in the oxide as a function of the local ion concentration and local electric field. Unfortunately, these relations are complicated, and closed form solutions for the overall transport and overall oxide field vs. oxide thickness can only be approximated, i.e., the problem must be solved numerically.<sup>11,26</sup>

The assumptions of Cobine's Law<sup>27,28</sup> for fully developed space-charge limited ionic transport are similar to the assumptions proposed in the hopping conduction, space-charge limited transport models. In Cobine's Law, the ions are assumed to have a constant mobility and suffer many collisions during transport across the space-charge layer. In terms of the MCM models, these assumptions are similar to assuming a constant hopping distance and uniform barrier height for hopping conduction. In Cobine's Law, the overall ion flux can be related to the film thickness and overall oxide potential drop by:<sup>27</sup>

$$j_i - \Gamma_i = \frac{9}{8} K_{ox} \epsilon_o \mu_i \left[ \frac{V_{ox}^2}{x_{ox}^3} \right] \quad (12)$$

where  $V_{ox} = (V_{app} - V_s)$ ,  $K_{ox}$  is the dielectric constant of the oxide (3.5 to 4),  $\epsilon_o$  is the permittivity of free space and  $\mu_i$  is the ion mobility. A plot of  $(j_i x_{ox}^3)$  vs.  $V_{ox}^2$  should therefore yield a straight line with slope  $(9/8)K_{ox}\epsilon_o\mu_i$  if Cobine's Law is applicable. The bottom portion of Fig. 9 shows this relation. Neglecting the initial regime,  $(j_i x_{ox}^3)$  is linear over a large span of  $V_{ox}^2$ , and the slopes for the two constant applied voltage conditions are nearly identical. The mobility extracted from these slopes was  $\approx 3 \times 10^{-11} \text{ cm}^2 \text{ V}^{-1} \text{ s}^{-1}$ . This value is nine orders of magnitude smaller than that predicted for the gas phase ion mobility (Eq. (5) in Reference 27). This substantial difference can be viewed as an addition term for hopping conduction probability in the solid state ( $\exp(W/k_B T)$ , where  $W$  is the hopping conduction barrier height and  $k_B$  is Boltzmann's constant) that is not included in the gas phase mobility calculation. (A hopping conduction energy barrier height of  $\approx 1 \text{ eV}$  yields a value of  $\exp(W/k_B T)$  at 623 K of  $8 \times 10^{-9}$ .)

If we assume that the solid-state ion mobility is roughly constant in the oxide for a given temperature (i.e., it is field independent and is the same under ohmic or space-charge limited transport conditions), then it can be related to the overall conductivity in the oxide by:

$$\eta \sigma = e n_i \mu_i \quad (13)$$

where  $n_i$  is the average ion concentration in the oxide. Using the value of  $4 \times 10^{-9} \Omega^{-1} \text{cm}^{-1}$  for the overall conductivity and  $1 \times 10^{-3}$  for the current efficiency (calculated in subsection C 1), Eq. (13) estimates  $n_i$  to be on the order of  $1 \times 10^{18} \text{cm}^{-3}$ . This value is close to the  $n_i$  estimated in GaAs anodization under constant current conditions, similar ion fluxes and electric field strengths.<sup>19</sup> Furthermore, the mean drift velocity,  $u \approx j_i/n_i$ , is on the order of  $375 \text{nm s}^{-1}$ , yielding an effective mean free path much smaller than  $x_{\text{ox}}$ , consistent with the assumptions of Cobine's Law. Thus, the observation in this study that  $V_{\text{ox}}$  increases non-linearly with increasing oxide thickness when space-charge effects become important, is consistent with this type of space-charge limited flow.

## VI. Oxide Physical Properties

The physical and chemical characteristics of the as-grown, positively biased (constant current or constant voltage) oxides of 60 nm or less thickness were identical to thermal oxides grown at 1123 K or higher in temperature. The refractive index of these ECR films was 1.467 - identical to thermal silicon dioxide. Etch rates in BOE solutions were identical to dry thermal oxides grown at 1123 K. FTIR, XPS and AES spectra revealed no observable chemical differences between thermal oxides and these positively biased ECR oxides. The position and full width half maximum of the  $1070 \text{cm}^{-1}$  Si-O IR absorbance peak were identical for both oxides if the oxides were grown at similar rates and the spectra were corrected for film thickness variations. For film thicknesses of approximately 60 nm and larger, a slight increase in BOE etch rate was observed, i.e., etch rate was 1.1 to 1.25 times that of the thermal oxide rate. This could possibly be due to film stress, or to general film degradation from the passage of electron current with time.

BOE etch rates of the oxides grown at the floating potential and the negatively biased, or cathodized oxides were much higher than the thermal oxide controls. BOE rates of 1.5 to 3 times the thermal oxidation rate indicated that these films were significantly different in film density or film porosity. The index of refraction for the floating potential films was 1.46. The negatively biased films exhibited much lower refractive indices (at or below 1.43) indicative of substantially reduced film

density.<sup>32</sup> FTIR analysis of these films did not show significant chemical differences from thermal oxides, as observed previously.<sup>3,7,14</sup> Thus, the most stringent physico-chemical analysis appears to be etch rate in BOE solutions.

TEM was used to compare ECR oxides grown under positive bias conditions to thermal oxides of equivalent thicknesses. Fig. 10 shows a micrograph of a 7 nm ECR oxide grown on <100> silicon with an evaporated aluminum gate on top of the oxide layer. The diffraction pattern inset in Fig. 10 is of the bulk crystalline silicon (looking into the <110> plane), far removed from interface effects. The oxide-silicon interface is as uniform as the thermal oxide-silicon interface observed in this and other studies.<sup>33,34</sup> and the oxide is uniform in thickness over extended areas ( $\approx 1\text{-}2\ \mu\text{m}$ ), as shown in the inset of Fig. 10. The 1 to 1.5 nm transition region from bulk crystalline silicon to the bulk oxide seen in Fig. 10 is consistent with that observed in thermal oxide samples. Furthermore, the oxide-aluminum interface is also uniform over long distances. No defects, pinholes, or areas of lower apparent oxide density have been observed in the positively bias ECR oxides thicker than 7 nm.

## VII. Oxide Electrical Properties

### A. Capacitance - Voltage Analysis

The electrical properties of the ECR oxides grown were strong functions of processing conditions and post-processing treatment. To analyze the as-grown properties, aluminum gates were used. Aluminum evaporation and sinter steps are performed at temperatures close to or below the oxidation temperature and thus process induced radiation damage annealing is minimized. The upper plot in Fig. 11 shows the high frequency C-V trace for three ECR oxides and a thermally grown oxide control, where the films were 20 to 30 nm thick. All as-grown ECR oxides had significant flatband shifts ( $\approx 1\ \text{V}$ , fixed charge ( $Q_{\text{ox}}$ )  $> 1 \times 10^{11}\ \text{cm}^{-2}$ ) and high levels of interface traps ( $D_{\text{it}} > 1 \times 10^{12}\ \text{cm}^{-2}\ \text{eV}^{-1}$  as determined by Terman's method<sup>35</sup>) compared to the thermal oxide control. Oxides grown at the floating potential exhibited a hysteresis of  $\approx 400\ \text{mV}$  upon sweeping from accumulation back into depletion. This "damage" may be due to uv photon flux and electron flux from the plasma. Mobile

ionic charges were not detected during bias temperature stressing.

When polysilicon was used as the gate metal, the effects of plasma induced radiation damage were significantly reduced. The bottom portion of Fig. 11 shows the high frequency C-V traces for both positive bias and floating potential films; the electrical properties calculated from these curves are listed in Table II. Polysilicon deposition and activation is a high temperature (1123 K) process. Since most uv radiation damage can be annealed out of the oxide below 730 K<sup>36</sup>, the oxide fixed charge,  $Q_{ox}$  is reduced to that of the thermal oxide control sample. However, significant ( $\approx 1 \times 10^{11} \text{ cm}^{-2} \text{ eV}^{-1}$ ) interface traps remained, even after these high temperature anneals. Although this interface trap density is undesirable for a gate dielectric, it is comparable to the low temperature (1123 K growth temperature) thermal oxide trapping levels observed in our controls and is within acceptable limits for device gate design. No mobile charges were detected in the bias temperature stress studies. The level and position of interface traps was also unaffected by bias temperature stressing.

It is interesting to note that the effective dielectric constant,  $K_{ox}$  for the thin gate ( $< 10 \text{ nm}$ ) ECR oxide capacitors ranged from 2-3, significantly less than the thicker gate value of 3.5 to 4. This was also true for the thermal oxide controls. Any charge leakage through the thin gate changes the observed accumulation capacitance ( $C_{ox}$ ). As the fields required to bring the capacitors into accumulation are on the order of several  $\text{MV cm}^{-1}$ , it is possible that leakage is responsible for the lower measured  $C_{ox}$  and thus lower effective  $K_{ox}$ . This should be true for any thin dielectric and thus both the thin thermal oxides and thin ECR oxides yield lower  $K_{ox}$  values.

## B. Current - Voltage Analysis

The cumulative dielectric breakdown vs. applied oxide field is shown for both aluminum gates and polysilicon gates in Fig. 12. The thermal oxide control exhibited intrinsic breakdown behavior, i.e., failure for all capacitors at approximately  $11 \text{ MV cm}^{-1}$ , for both gate metals, and thus was unaffected by the different gate metal process flows. ECR oxides exhibited a low mean breakdown field strength (MBDF) after aluminum gate evaporation and sintering. MBDF in the ECR oxides post

polysilicon gate deposition and activation was significantly higher. The intrinsic breakdown field (the portion of the MBDF curve with steep slope in Fig. 12) for the ECR oxides with polysilicon gates was high, at or above the thermal oxide intrinsic breakdown level. However, ECR oxides exhibited low field (5-8 MV cm<sup>-1</sup>) breakdown behavior for 10-30% of the devices tested in both gate metallization sequences. Some of this "spread" in the MBDF may be attributed to the slight film thickness non-uniformity (2-4%, one standard deviation) and the lack of particle-free clean room conditions during wafer handling prior to and post ECR processing. However, some of the of the spread in distribution is believed to be due to the residual radiation damage induced by the plasma.

### **VIII. Conclusions**

Oxides with physical characteristics identical to thermal oxides and electrical characteristics acceptable for device manufacture were grown under positive bias conditions in an ECR oxygen plasma. Oxides grown under floating potential conditions or under negative bias had inferior as-grown physical and electrical properties. Analysis of the growth kinetics and applied potentials during constant current anodization showed that there are three distinct oxidation regimes: initial parabolic growth; linear growth in the ohmic regime; and space-charge limited growth. The linear rate coefficient for constant current anodization at 0.13 Pa was proportional to the square root of the gas phase atomic oxygen concentration. Current efficiencies calculated from constant current anodizations in the linear regime of growth were consistent with those calculated from constant voltage anodization growth rates. Scaling of the oxide potential drop with oxide thickness in the space-charge limited regime was similar to the theoretical scaling law for space-charge limited collisional ion transport.

## **Acknowledgements**

This work was supported by National Science Foundation Grants No. ECS-8517363 and No. ENG-8710988, Department of Energy Grant Nos. DE-FG03-87ER13727 and DE-ACO3-76SF00098, Dept. of Defense Contract No. F49620-87-K-0001, and a contract from IBM General Technology Div., Burlington, VT. Helpful insight from Dr. Paul Landler of IBM General Technology Division is gratefully acknowledged.

## References

1. J. Kraitchman, *J. Appl. Phys.* **38**, 4223 (1967).
2. D. L. Pulfrey, F. G. M. Hathorn, and L. Young, *J. Electrochem. Soc.* **120**, 1529 (1973).
3. D. L. Pulfrey and J. J. Reche, *Sol. State Elec.* **17**, 627 (1974).
4. L. Bárdoš, J. Musil, F. Zacek, and L. Hulenyi, *Czech. J. Phys.* **B 28**, 639 (1978).
5. S. Gourrier and M. Bacal, *Plasma Chem. and Plasma Proc.* **1**, No. 3, 217 (1981).
6. A. K. Ray and A. Reisman, *J. Electrochem. Soc.* **128**, 2460 (1981) and *J. Electrochem. Soc.* **128**, 2466 (1981).
7. S. Kimura, E. Murakami, K. Miyake, T. Warabisaka, H. Sunami and T. Tokuyama, *J. Electrochem. Soc.* **132**, 1460 (1985).
8. C. Vinckier, P. Coeckelberghs, G. Stevens and S. De Jaegerer, *Appl. Surf. Sci.* **30**, 40 (1987) and *J. Appl. Phys.* **62**, 1450 (1987).
9. J. L. Moruzzi, A. Kiermasz, and W. Eccleston, *Plasma Phys.* **24**, 605 (1982).
10. A. Kiermasz, W. Eccleston, and J. L. Moruzzi, *Solid State Electronics* **26**, 1167 (1983).
11. S. Taylor, W. Eccleston, and K. J. Barlow, *J. App. Phys.* **64**, 6515 (1988).
12. T. Roppel, D. K. Reinhard, and J. Asmussen, *J. Vac. Sci. Tech.* **B 4**, 295 (1986).
13. G. T. Salbert, D.K. Reinhard and J. Asmussen, *J. Vac. Sci. Tech.* **A 8**, 2819 (1990).
14. D. A. Carl, D. W. Hess, and M. A. Lieberman, *J. Vac. Sci. Tech.* **A 8**, 2924 (1990).
15. D. A. Carl, D. W. Hess, and M. A. Lieberman, *J. Appl. Phys.* **68**, 1859 (1990).
16. R. Walkup, K. Saenger, and G. S. Selwyn, *Mat. Res. Soc. Symp. Proc.* **38**, 69 (1985).
17. D. A. Carl, M. C. Williamson, M. A. Lieberman and A. J. Lichtenberg, *J. Vac. Sci. Tech.* **B**, March/April (1991) - (to be published).
18. J. F. O'Hanlon, in *Oxides and Oxide Films*, edited by A. K. Vijh, Marcel Dekker Inc., New York, New York, Vol 5, pp. 110-121 and 140-151 (1977).
19. P. Friedel, S. Gourrier, and P. Dimitriou, *J. Electrochem. Soc.* **128**, 1857 (1981).

20. N. Cabrera and N. F. Mott, *Rept. Prog. Phys.*, **12**, 163 (1948).
21. D. R. Wolters and A. T. A. Zegers-van Duynhoven, *J. Appl. Phys.* **65**, 5126 (1989).
22. P. J. Jorgensen, *J. Chem. Phys.* **37**, 874 (1962).
23. E. A. Irene and E. A. Lewis, *App. Phys. Lett.* **51**, 767 (1987).
24. E. M. Young, *Appl. Phys. A.* **47**, 259 (1988).
25. T. G. Mills and F. A. Kroger, *J. Electrochem. Soc.* **120**, 1582 (1973).
26. A. T. Fromhold, Jr., in *Oxides and Oxide Films*, edited by A. K. Vijh, Marcel Dekker Inc., New York, New York, Vol. 3 pp. 109-110 and 144-147, (1976).
27. M. A. Lieberman, *J. App. Phys.* **65**, 4186 (1989).
28. J. D. Cobine, *Gaseous Conductors*, Dover, New York, New York, p. 128 (1941).
29. C. Vinckier and S. De Jaegere, *J. Electrochem. Soc.* **137**, 628 (1990).
30. Y. Yasuda, S. Zaima, T. Kaida, and Y. Kiode, *J. App. Phys.* **67**, 2603 (1990).
31. E. J. Verwey, *Physica* **2**, 1059 (1935).
32. W. A. Pliskin, *J. Vac. Sci. Tech.* **14**, 1064 (1977).
33. A. Ogura, *Semiconductor Silicon 1990*, Proc. of the Sixth Int. Symp. on Silicon Mat. Sci. and Tech. The Electrochemical Society, Pennington, New Jersey, Vol. 90-7, 332 (1990).
34. A. Kalnitsky, S. P. Tay, J. P. Ellul, S. Chongsawangvirod, J. W. Andrews and E. A. Irene, *J. Electrochem. Soc.* **137**, 234 (1990).
35. E. H. Nicollian and J. R. Brews, *MOS (Metal Oxide Semiconductor) Physics and Technology*, John Wiley and Sons, New York, New York, 156-165 (1982).
36. B. E. Deal, *J. Electrochem. Soc.* **121**, 198C (1974).

## Figure and Table Captions

- Fig. 1: Schematic of biasing system used in this study.
- Fig. 2: I-V characteristics of the wafer holder in a  $P_{\text{forward}} = 500 \text{ W}$ , 0.13 Pa oxygen discharge along with normalized ion density (solid squares), measured 1 cm in front of the wafer holder during the I-V sweep and normalized 525.5 nm  $\text{O}_2^+$  optical emission intensity (solid triangles) simultaneously measured in the source region.
- Fig. 3: Bias application schematic and subsequent potential profiles in the growing film for: a) constant current operation; and b) constant positive applied voltage operation.
- Fig. 4: Oxide thickness vs. oxidation time for the floating case at four different temperatures with a parabolic fit from Eq. (4) (solid line) and the associated plot of oxide thickness standard deviation vs. oxide thickness.
- Fig. 5: Oxide thickness vs. oxidation time for constant current anodization for four different system pressures.
- Fig. 6: Applied bias,  $V_{\text{app}}$  as a function of oxide thickness for the constant current anodizations shown in Fig. 5.
- Fig. 7: Normalized linear rate for constant current anodizations ( $-20 \text{ mA cm}^{-2}$ ) vs. actinometrically estimated atomic oxygen concentrations performed at 0.13 Pa total pressures for various oxygen/argon mixtures and for changes in total power for pure oxygen operation.
- Fig. 8: Oxide thickness vs. time for two constant positive bias operation cases and associated calculated oxidation rates vs. total negative current drawn.
- Fig. 9: Ohmic and Cobine's Law plots for the constant applied bias conditions shown in Fig. 8.

- Fig. 10: TEM cross section of a 7 nm ECR oxide, grown under constant positive bias conditions. The image is a small portion of the 0.4  $\mu\text{m}$  wide section shown in the inset. The inset diffraction pattern is of the  $\langle 110 \rangle$  crystal plane of the bulk silicon.
- Fig. 11: High frequency C - V curves for various bias conditions ECR oxides and for two different gate metals. The solid line is a thermal oxide control.
- Fig. 12: Cumulative breakdown percentage vs. applied field for various ECR growth conditions and for two different gate metals. The thermal oxide control sample exhibited breakdown a 11  $\text{MV cm}^{-1}$  both gate metals.
- Table I: Parabolic, linear and power law fit parameters as well as linear current efficiency,  $\eta$ , for constant current ( $-20 \text{ mA cm}^{-2}$ ) anodizations performed at  $P_{\text{forward}} = 500 \text{ W}$  and various system pressures.
- Table II: C - V and I - V electrical testing summary for polysilicon MOS capacitors.

Table I

Pressure	$k_5$	$x_{ox}(t=0)$	$k_6$	$\eta \times 10^3$	$\sigma \times 10^9$	$C^*$	$\alpha$
(Pa)	( $\text{nm}^2 \text{min}^{-1}$ )	(nm)	( $\text{nm min}^{-1}$ )		( $\text{\AA}^{-1} \text{cm}^{-1}$ )	( $\text{nm min}^{-\alpha}$ )	
0.033	29.38	5.38	1.74	1.05	21.5	2.20	0.932
0.130	26.07	4.63	2.45	1.48	4.90	3.74	0.812
0.260	13.82	4.52	1.79	1.08	4.07	3.05	0.844
1.300	17.56	2.79	1.59	0.96	7.68	2.96	0.735

Table II

Pressure (Pa)	$x_{\text{ox}}$ (nm)	$V_{\text{app}}$ (V)	Fixed Charge, $Q_{\text{ox}}$ ( $\times 10^{10} \text{ cm}^{-2}$ )	$K_{\text{ox}}$	$D_{\text{it}}$ , mid gap ( $\times 10^{11} \text{ cm}^{-2} \text{ eV}^{-1}$ )	MBDF ( $\text{MV cm}^{-1}$ )
0.130	5.4	+5	4.82	2.41	1.87	$10.87 \pm 0.83$
0.130	8.8	+5	4.33	2.75	0.92	$10.02 \pm 1.42$
0.130	5.3	Floating	0.76	2.54	2.64	$10.73 \pm 1.89$
0.033	9.0	+2	10.75	2.98	2.31	$10.88 \pm 2.20$
1.300	8.5	+10	4.38	3.03	0.91	$8.67 \pm 1.90$
Thermal Oxide	8.0	-	4.71	2.07	0.86	$11.16 \pm 0.13$

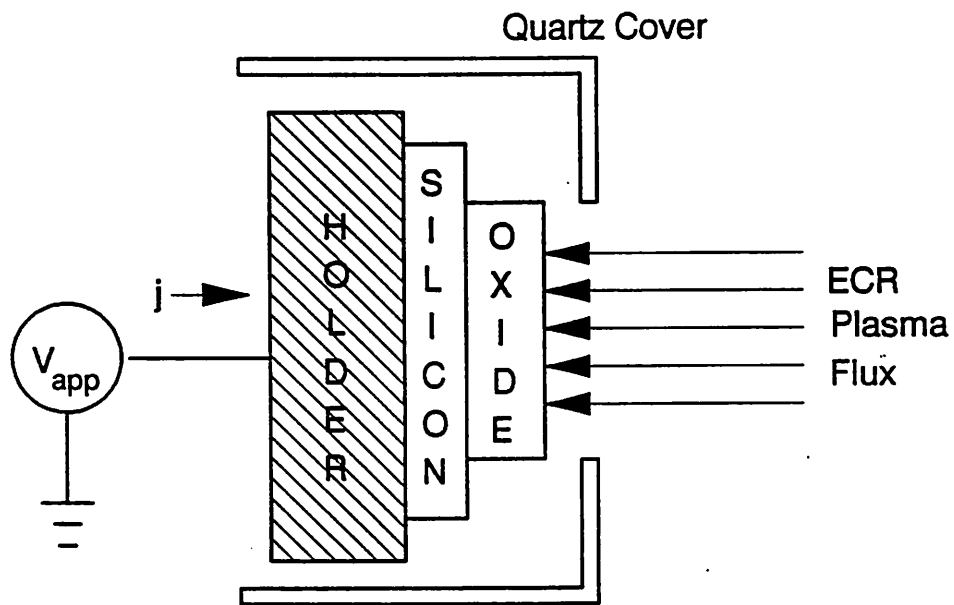


Fig. 1

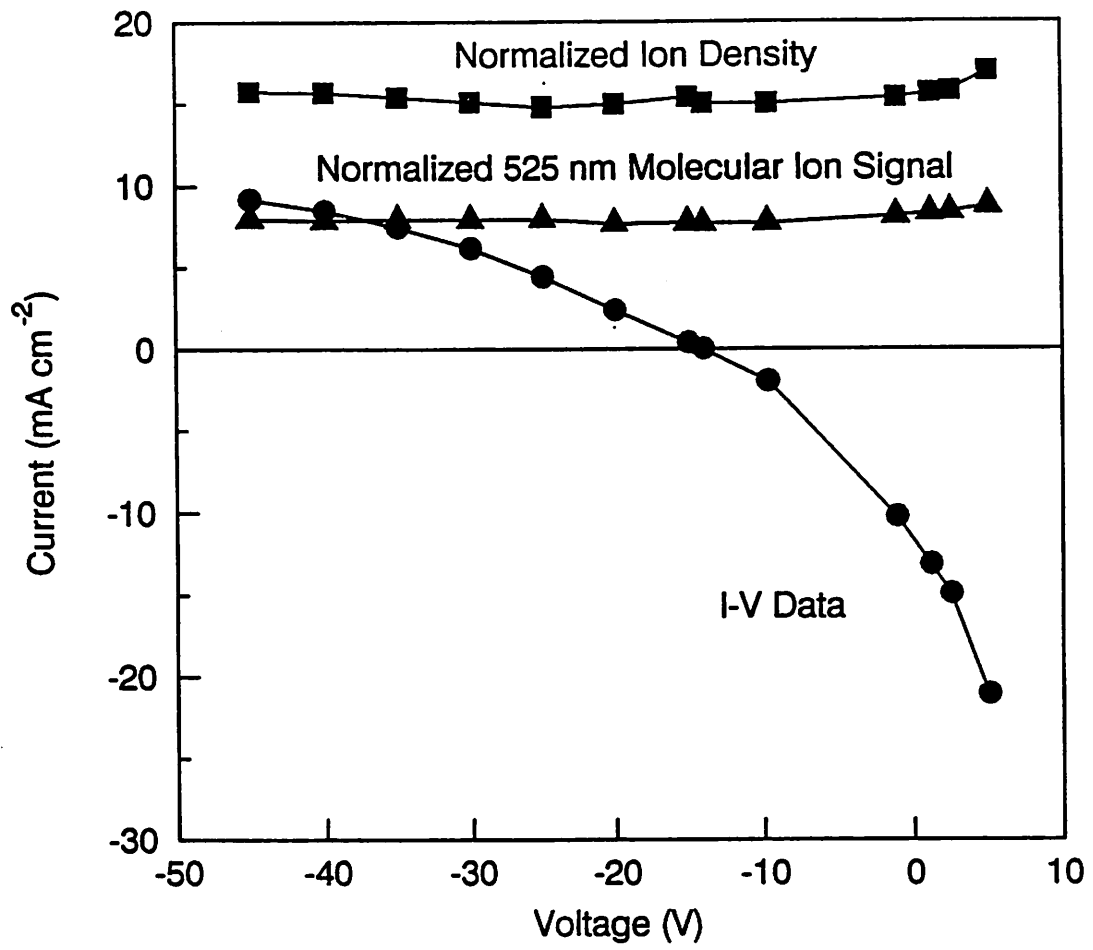


Fig. 2

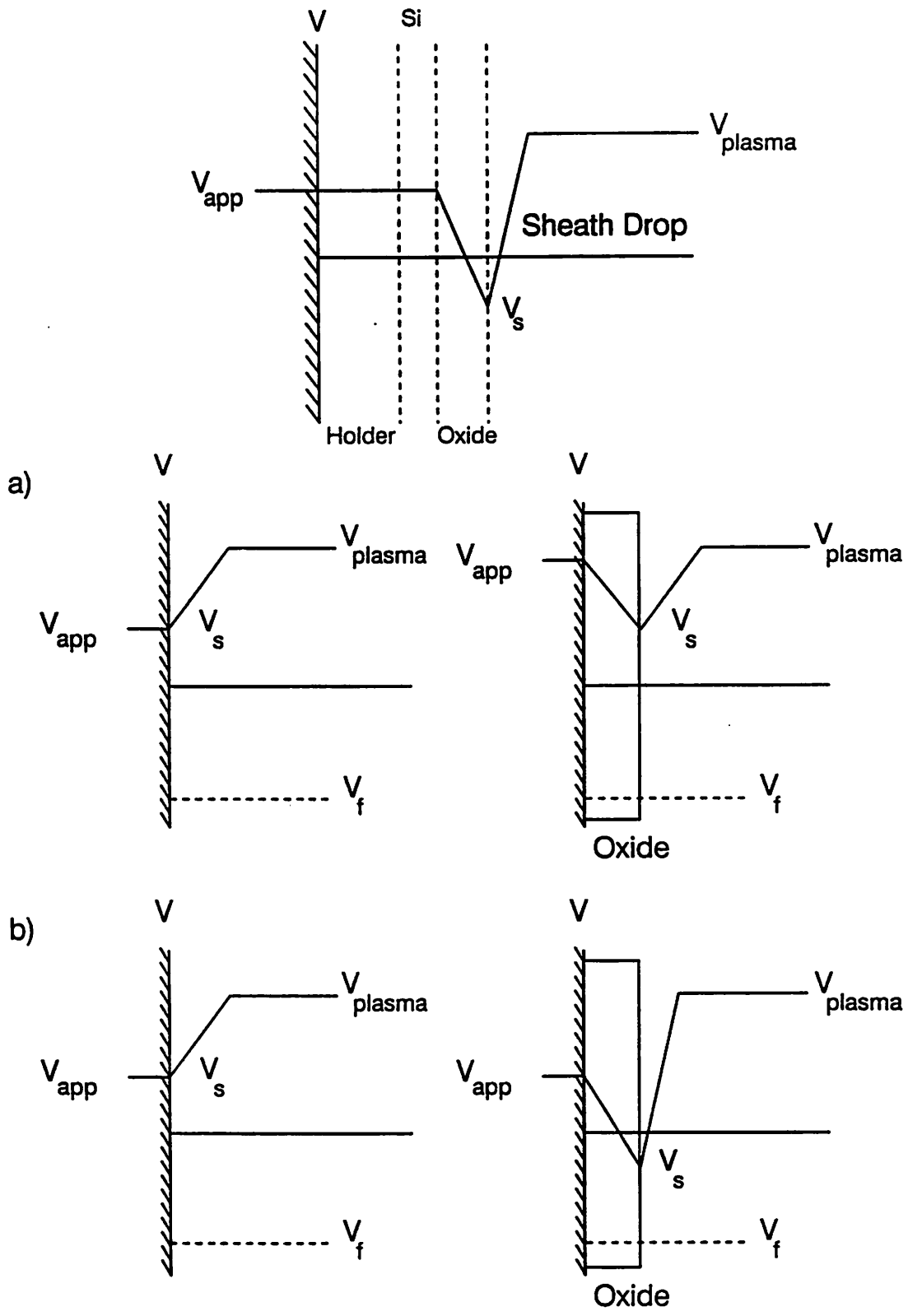


Fig. 3

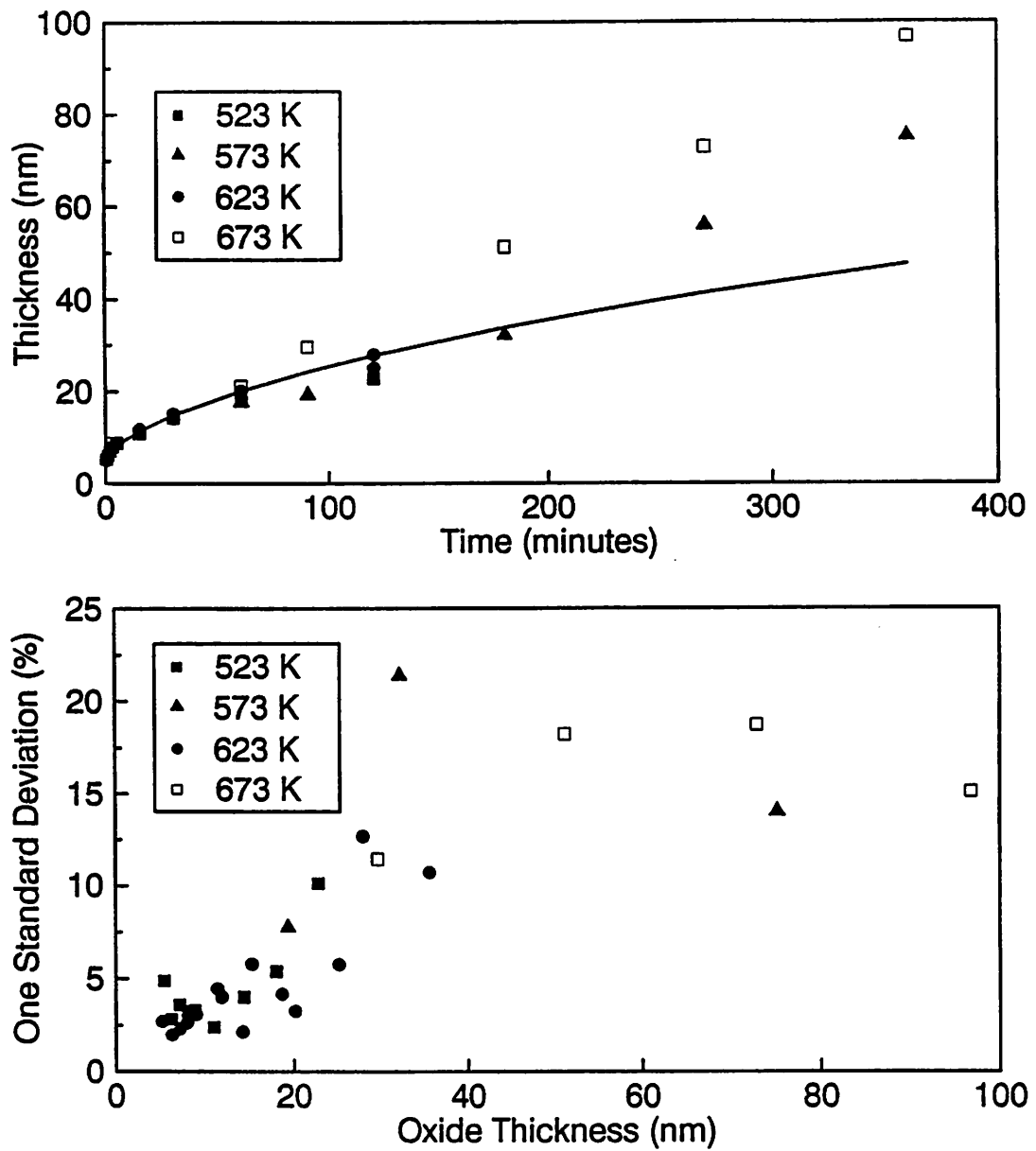


Fig. 4

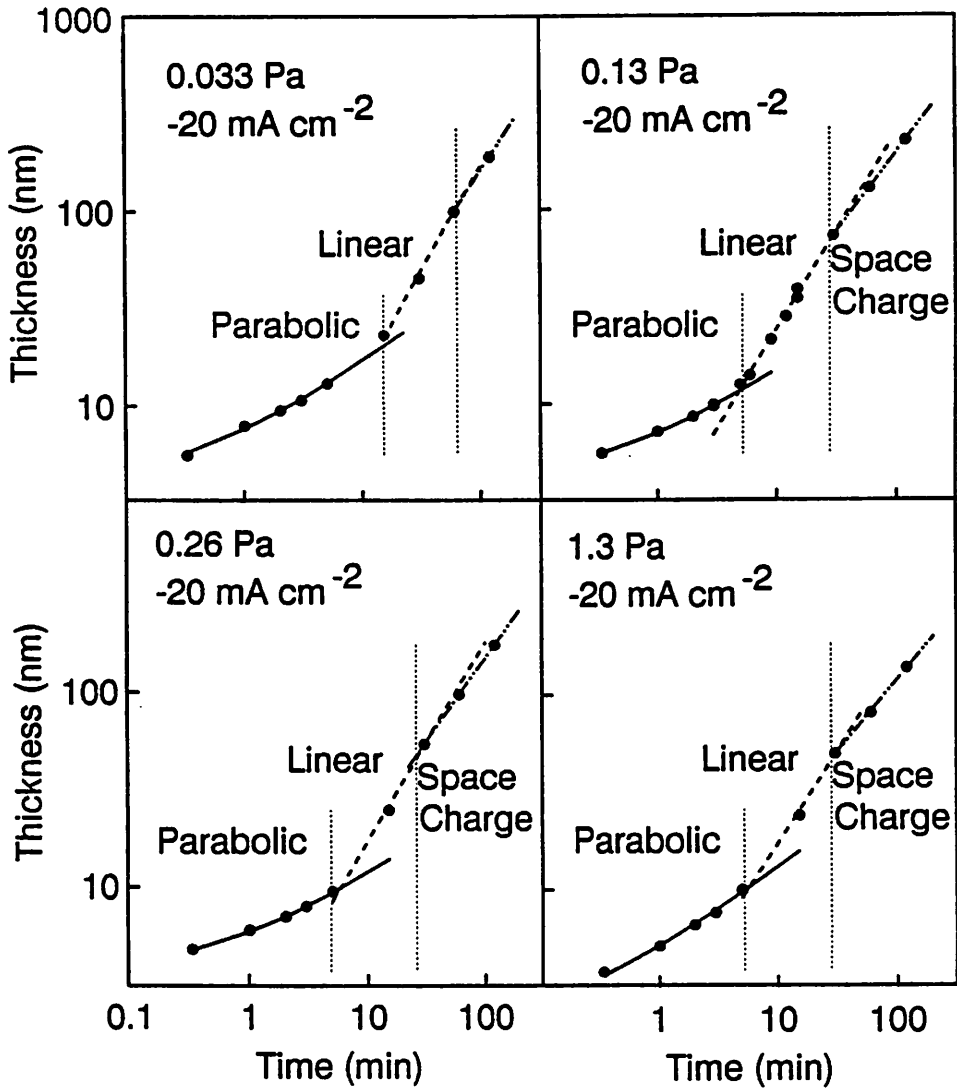


Fig. 5

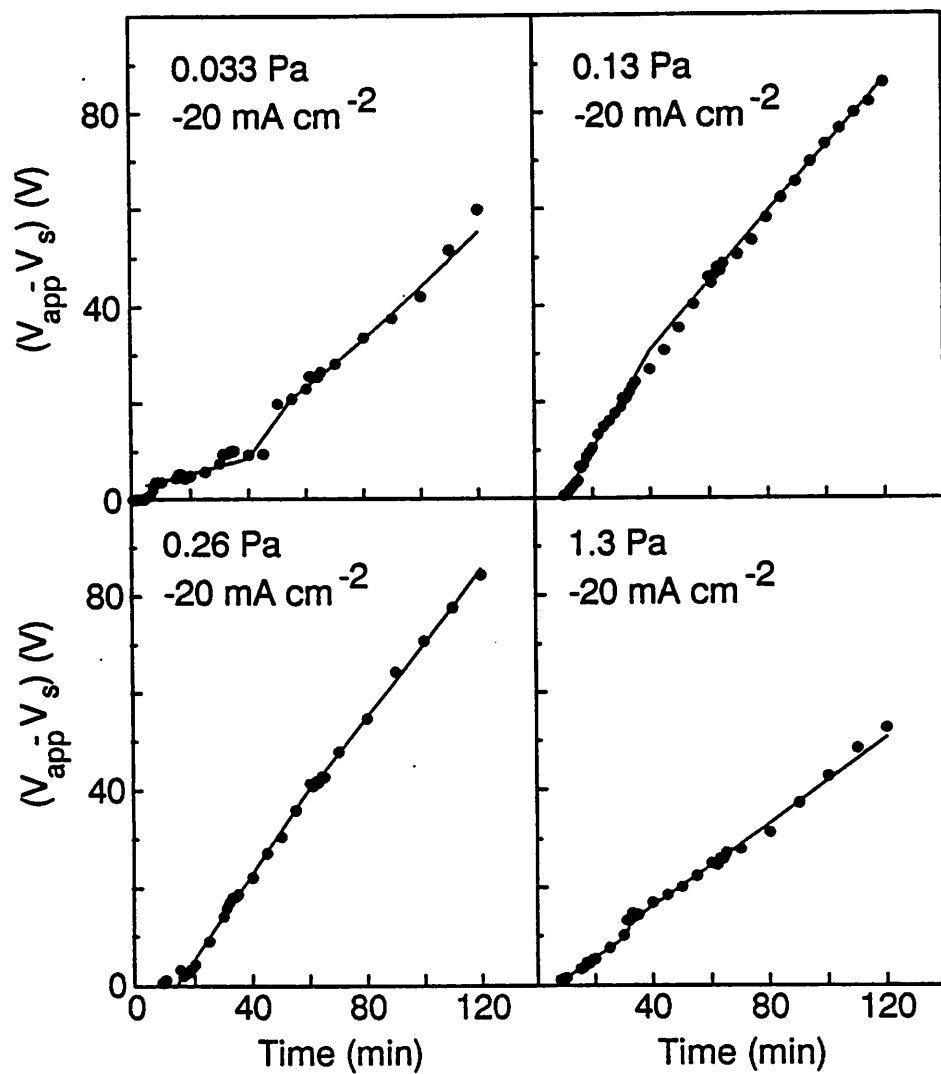


Fig. 6

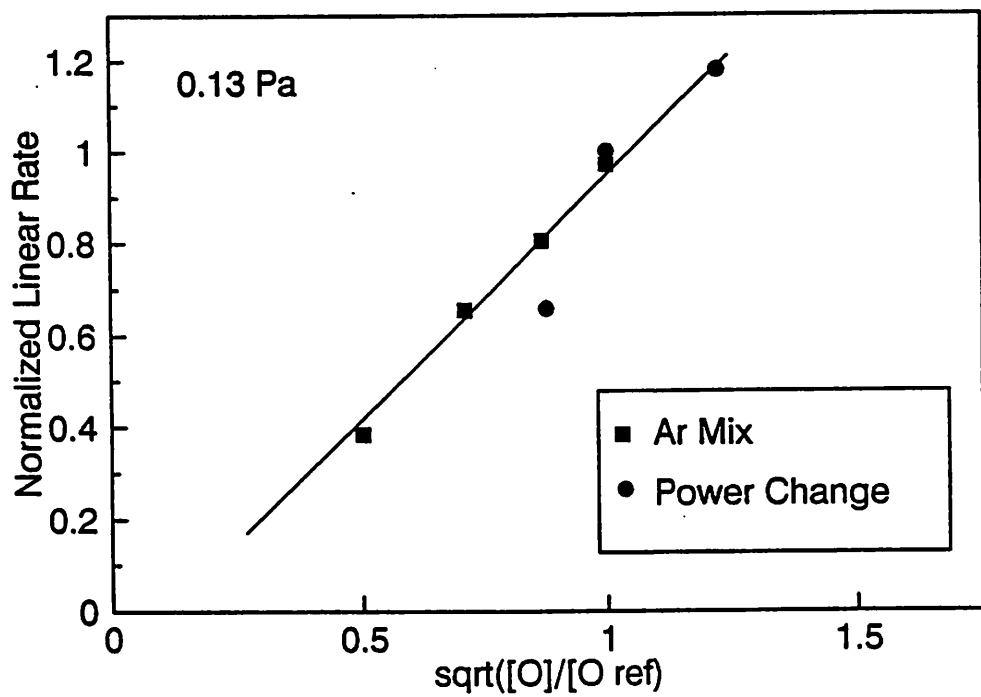
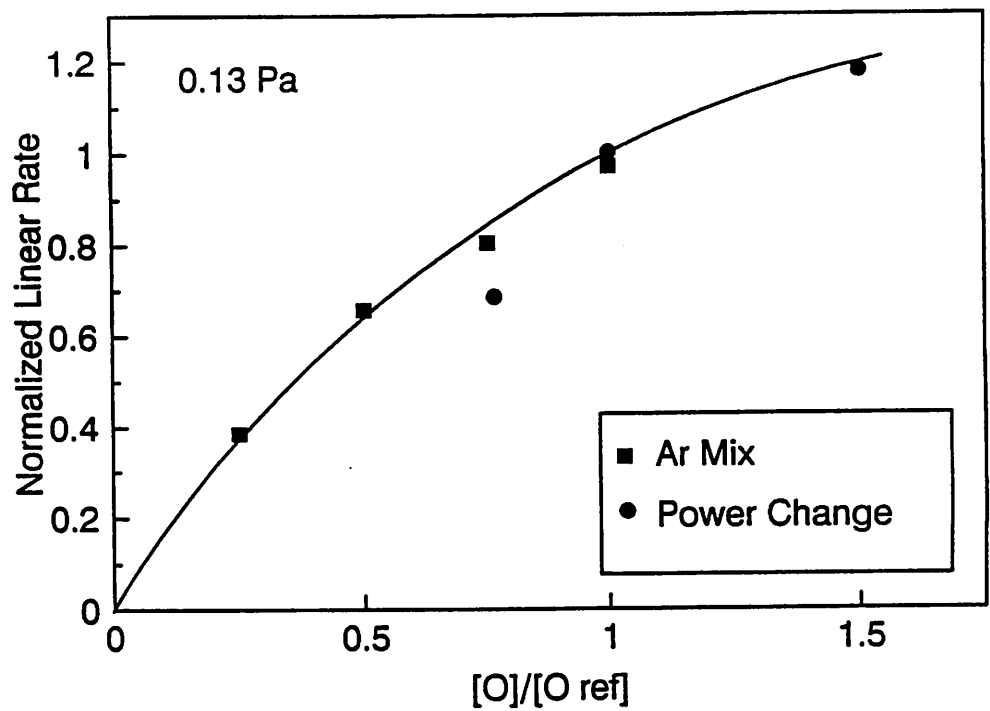


Fig. 7

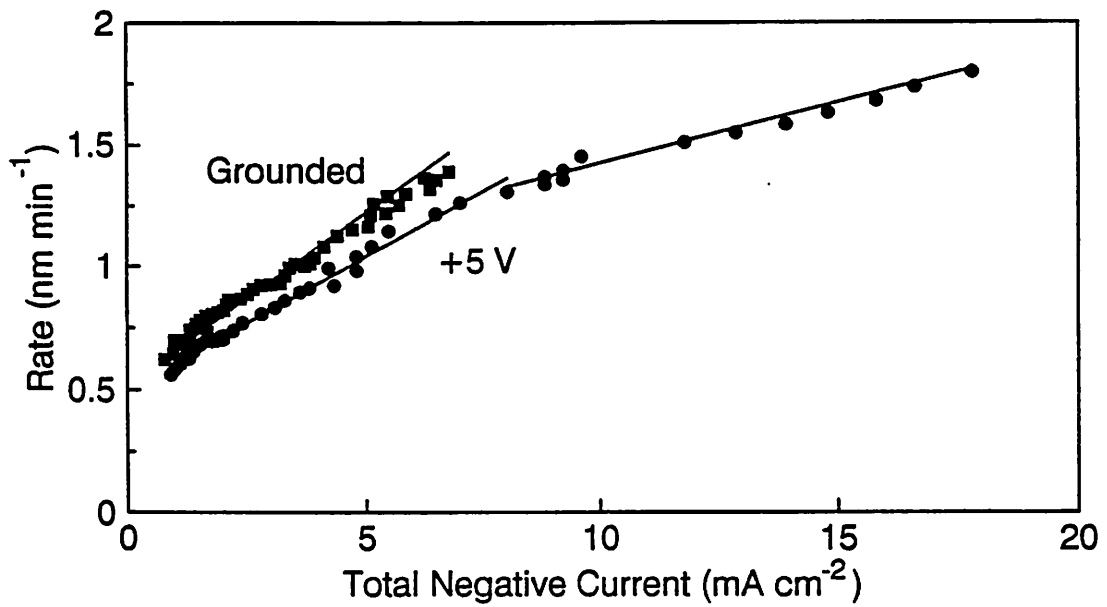
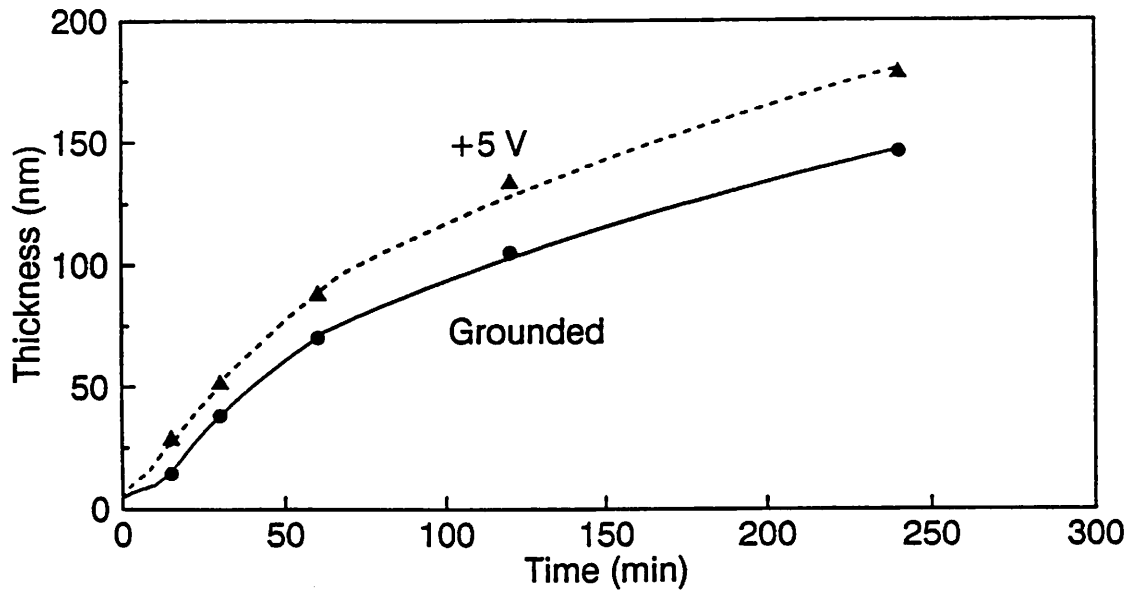


Fig. 8

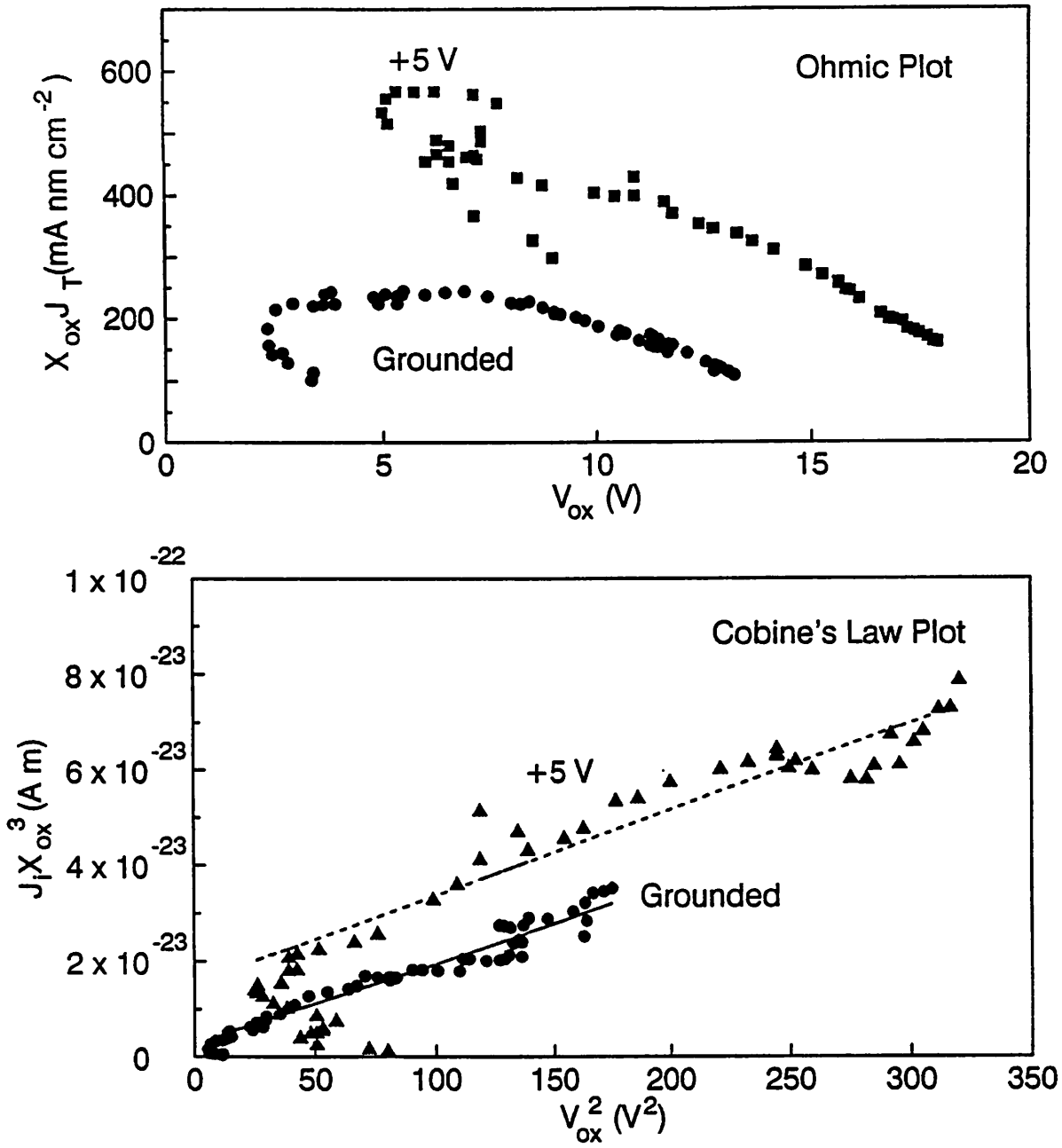
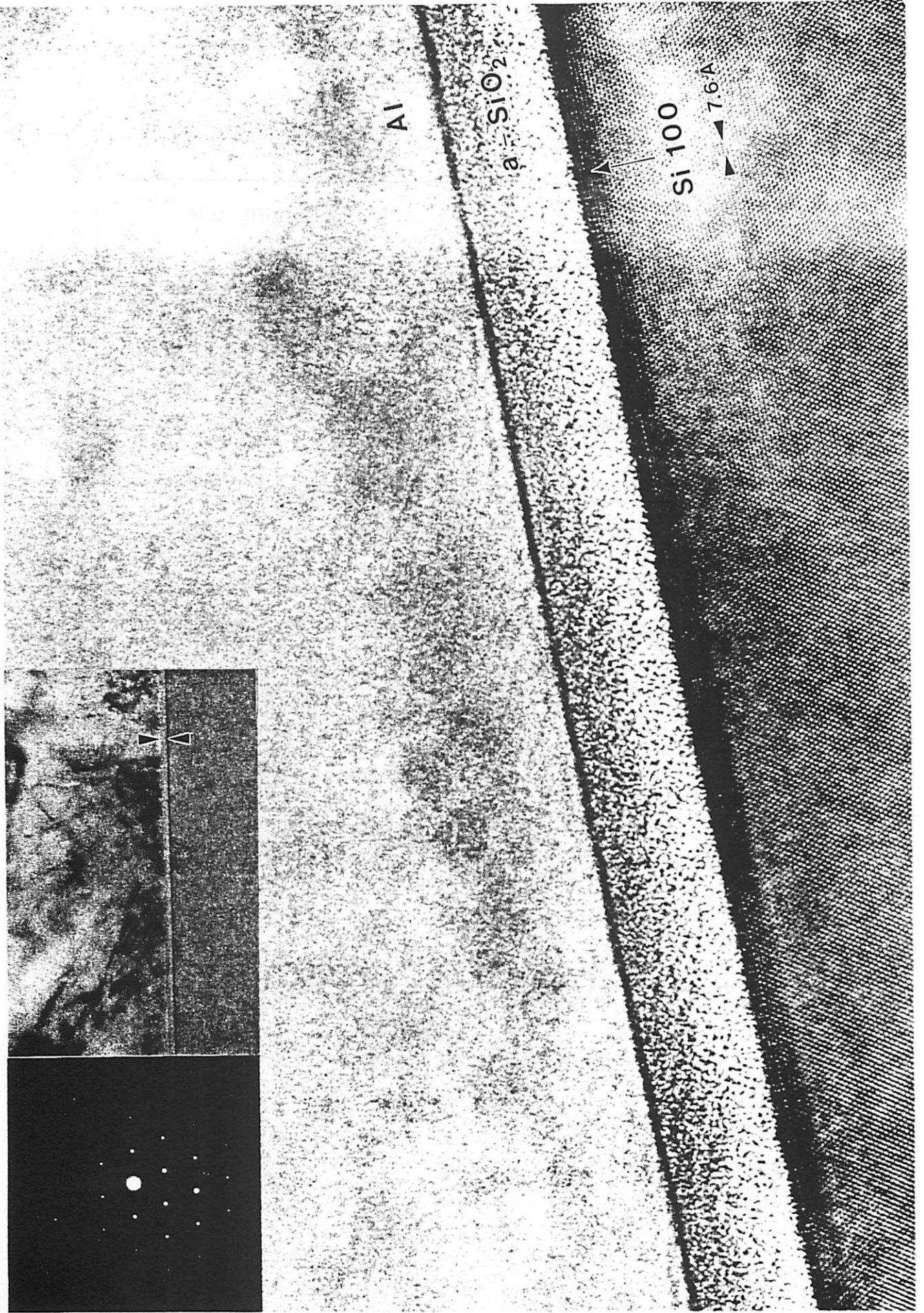


Fig. 9



41

FIG 10

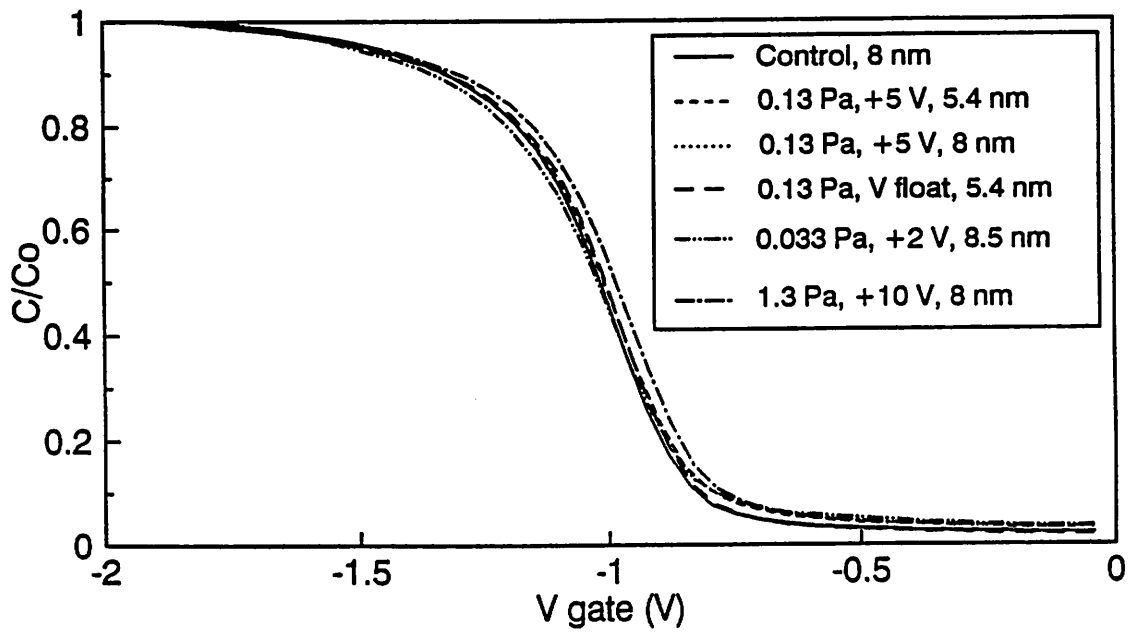
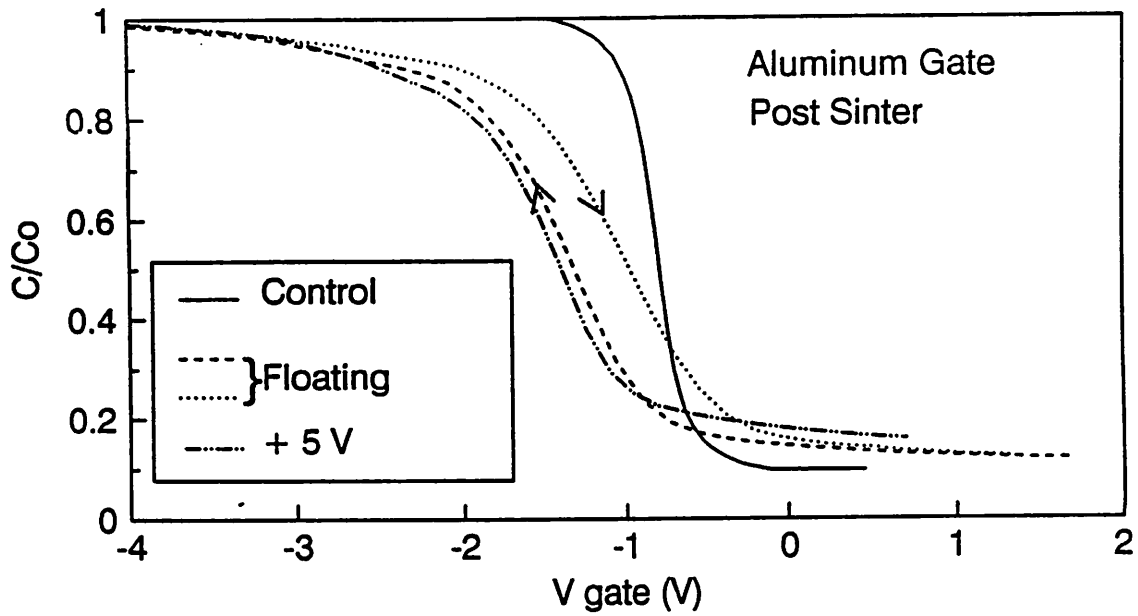


Fig. 11

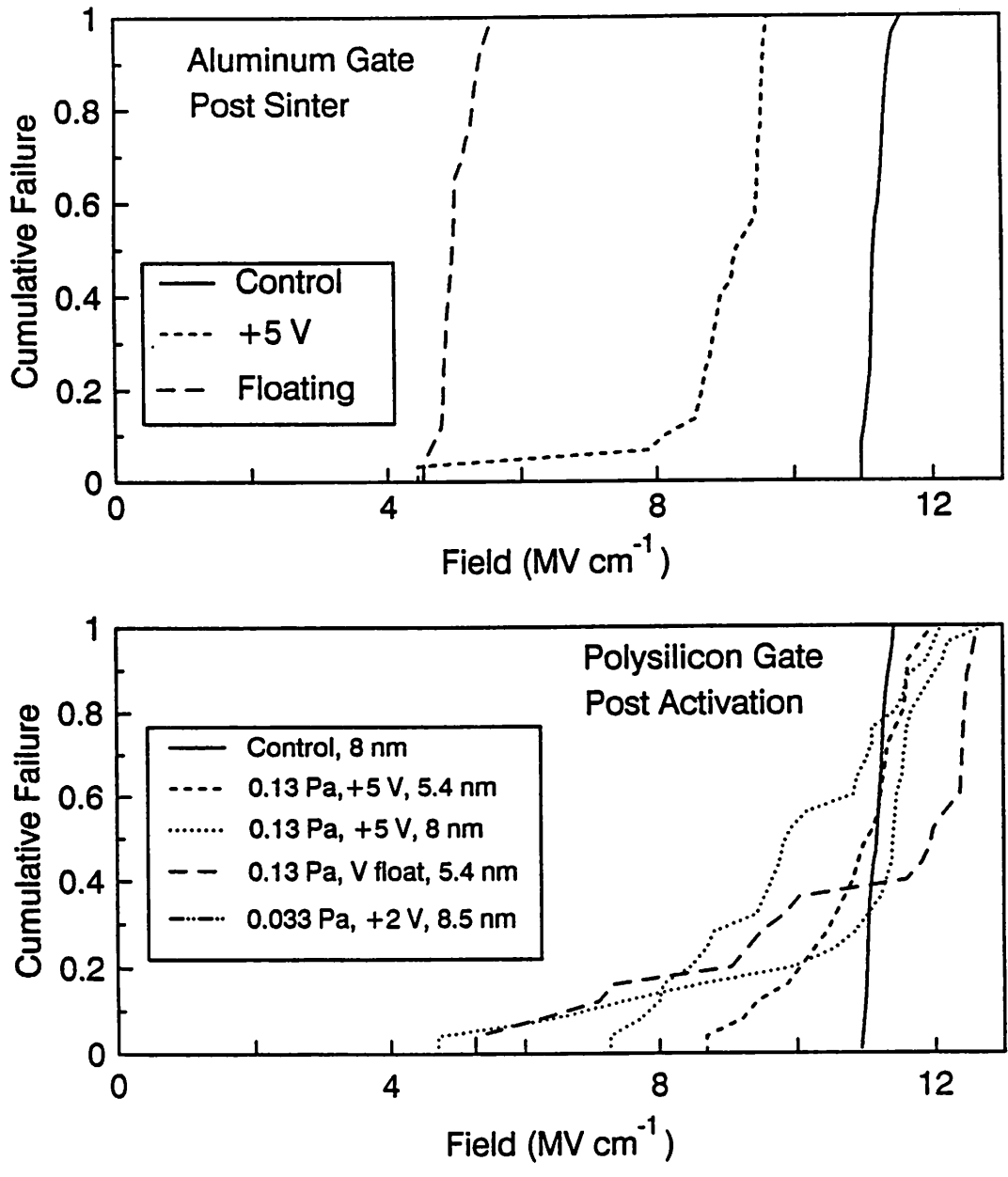


Fig. 12